

Spatial Verification of a Coordinate Measuring Machine Using a Renishaw Machine Checking Gauge

Dev Kumar, Thien Ho

▶ **To cite this version:**

Dev Kumar, Thien Ho. Spatial Verification of a Coordinate Measuring Machine Using a Renishaw Machine Checking Gauge. Independent research; original project at École Nationale Supérieure d'Arts et Métiers. 2026, pp.1-32. ⟨hal-05873045⟩

HAL Id: hal-05873045

https://hal.science/view/index/docid/5873045

Submitted on 19 Nov 2026

HAL is a multi-disciplinary open access archive for the deposit and dissemination of scientific research documents, whether they are published or not. The documents may come from teaching and research institutions in France or abroad, or from public or private research centers.

L'archive ouverte pluridisciplinaire **HAL**, est destinée au dépôt et à la diffusion de documents scientifiques de niveau recherche, publiés ou non, émanant des établissements d'enseignement et de recherche français ou étrangers, des laboratoires publics ou privés.



Copyright - All rights reserved

Spatial Verification of a Coordinate Measuring Machine Using a Renishaw Machine Checking Gauge

Planar form measurements, spatial error identification
and a reproducible numerical study

Dev KUMAR and Thien HO

École Nationale Supérieure d'Arts et Métiers

Lille, France

2024 engineering project
Experimental records and numerical study

Abstract

A 2024 coordinate measuring machine (CMM) experiment used a 151 mm Renishaw Machine Checking Gauge to compare planar and spherical probing paths. Four CALYPSO plots report circularity values of 1.10–1.49 µm. The reversal runs averaged 1.430 µm and the single-direction runs 1.115 µm. The archives provide the plots and the spatial fit estimates, with no matched scalar deviations or timing records to isolate hysteresis. The nominal ten-ring design identifies seven scaled coefficients with a condition number of 3.81. Two reported synthetic angular results differ from the inputs by factors of 98.79 and 9.88. The recovered generator omits angular terms in one branch. A controlled replay quantifies the omission, and further tests examine incomplete coverage, coordinate centring, exact radial intersection and correlated ring noise. A separate simulation of opposite-direction scans illustrates why both start order and station timestamps matter when estimating drift. Equal-area sampling and diagnostic filtering are evaluated with explicit point budgets and harmonic gains. The study provides reproducible calculations and retains the original measurement traces, equations and software excerpts.

Keywords coordinate measuring machine, Machine Checking Gauge, circularity, spatial error, squareness, identifiability, reversal, measurement uncertainty.

Study record

The campaign and original derivations are from the 2024 French report [1]. The English project report [2] adds the metrological framework and related plots. Original experimental images appear in Section 3. The figure concordance and formula facsimiles appear in Appendices A–B and the original code screenshots in Appendix C. Appendix D describes the embedded sources and reproducible Python study.

Acknowledgements

Thierry Coorevits supervised the project at École Nationale Supérieure d’Arts et Métiers, Lille.

Nomenclature

Symbol	Meaning
CMM, MCG	Coordinate measuring machine and Machine Checking Gauge
R, ρ, c	Nominal arm radius, latitude-ring radius and reference pivot
θ, φ, s	Azimuth, elevation and sine of elevation for surface integration
p, n, q, ε	Nominal point, unit normal, reconstructed point and normal deviation
N, M, N_θ	Observation or azimuthal count, ring count and azimuthal count per ring
d_c, s_c	Station chord and sagitta of a chord relative to the arc
u, v, w, δR	Local centre displacement components and effective radius difference
α, β, γ	Small shear angles in YZ, XZ and XY under Eq. (4.4)
X, T, S	Physically scaled model and its translation/radius and shear blocks
b, r, η, κ	Scaled coefficients, fit residual, observation disturbance and spectral condition number
H_{RMS}, H_{pp}	RMS and peak-to-peak matched directional differences
u_c, U, k	Combined standard uncertainty, expanded uncertainty and coverage factor

Contents

Abstract 1
Study record 1
Acknowledgements 1
Nomenclature 1
1. Project and measurement geometry 3
1.1 Research questions 3
1.2 Gauge, contact and reference frame 3
1.3 Unit normal and scalar displacement 4
1.4 Planar and spherical trajectory 4
1.5 Chord travel and fork clearance 5
2. Experiment and data reduction 6
2.1 Generation and CALYPSO input 6
2.2 Planar and spatial sequence design 7
2.3 Association and comparable endpoints 7
2.4 Reference temperature and uncertainty 8
3. Planar measurements and direction history 8
3.1 The four original traces 8
3.2 Field labels and descriptive comparison 10
3.3 Sensitivity of an extreme range to sample count 10
3.4 Paired differences and within-run time 11
4. Spatial error identification 12
4.1 Radius and centre from a radial observation 12
4.2 Sign convention for small squareness 13
4.3 Scaling, joint solution and staged projection 13
4.4 Reading rank and singular values 13
4.5 Coefficient uncertainty and robust estimation 14
5. Audit of the archived spatial estimates 15
5.1 The original recovery experiment 15
5.2 What the recovered code establishes 16
5.3 Independent tests of the estimator 16
5.4 The four reported fits to CMM records 17
6. Coverage, sampling and signal analysis 18
6.1 Spherical area and missing directions 18
6.2 Choice of ring distribution 19
6.3 What the legacy MATLAB routine subtracts 19
6.4 Hampel and Savitzky–Golay diagnostic view 20
7. Verification protocol and findings 21
7.1 Repeatable measurements 21
7.2 Conclusions 22
References 22
Appendix A. Original figure concordance 23
Appendix B. Original equations 24
Appendix C. Original software excerpts 26
Appendix D. Reproducibility and data fields 31

1. Project and measurement geometry

1.1 Research questions

The 2024 project used a Renishaw Machine Checking Gauge (MCG) on a ZEISS coordinate measuring machine (CMM) to develop circular and spherical probing paths [1]. Its two objectives were to characterise the response of the machine to changes in traversal direction and to extend the regions sampled during periodic verification [12]. The experiment used a nominal 151 mm arm. The four planar CALYPSO outputs and four sets of spatial coefficients survive in the reports [1, 2]. The individual point deviations and timing records were unavailable for this analysis.

Three questions structure the study. Do the four planar circularity values isolate a direction effect? Which combinations of translation, radius and axis geometry are observable in the spatial path? How do point density, time ordering and processing change the answer? The original results are transcribed directly. Independent calculations use declared synthetic inputs and are identified as such in each figure and table. The resulting distinctions matter because a modification of a CMM error map requires independent metrological validation.

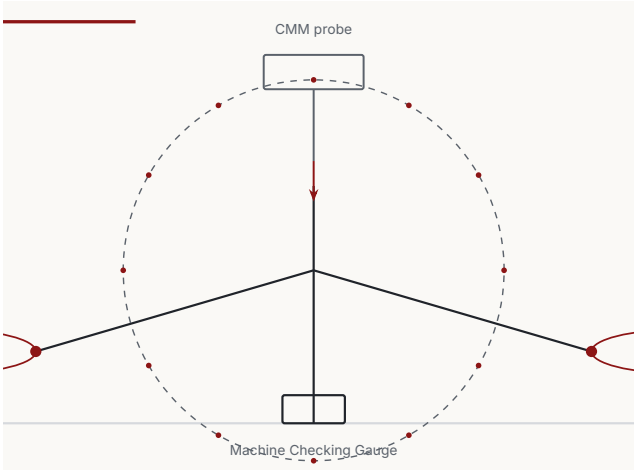

Figure 1.1 – Schematic of the CMM probe and Machine Checking Gauge from the English project report [2].

1.2 Gauge, contact and reference frame

The MCG arm rests in a kinematic seat on a pivot ball. Its measuring end supplies another kinematic contact with the stylus ball. The manufacturer describes a nominal 360° horizontal sweep and an elevation range of ±45° [3]. The available radii in the kit are 101, 151, 226, 380, 532 and 685 mm. Nominal arm length, calibrated arm length, stylus-ball radius and fitted circle radius are four distinct quantities. Only the nominal arm length of 151 mm is used in the calculations below.

The project photograph shows the gauge on the CMM table. The device characterises the combined response of the machine, probe and artefact in the sampled region. A CMM used to measure linear dimensions and a contacting probing system have specified acceptance and reverification tests in the relevant parts of ISO 10360 [4, 5]. Replacing those tests would require the prescribed measurands, configurations and decision rules.



Figure 1.2 – MCG mounted on the table below the ZEISS probe in the 2024 campaign [1, 2].



Figure 1.3 – Renishaw product image of the MCG assembly as reproduced in the project record [1, 2]. The operating principle is described by Renishaw [3].

1.3 Unit normal and scalar displacement

Let R be the nominal radius, c the local pivot at which the reference data are centred and n_i the unit radial normal. The geometry and the assumed sign of the normal deviation give

$$\begin{aligned} \mathbf{p}_i &= \mathbf{c} + R\mathbf{n}_i, \quad \|\mathbf{n}_i\|_2 = 1, \\ \mathbf{q}_i &= \mathbf{p}_i + \varepsilon_i \mathbf{n}_i. \end{aligned} \tag{1.1}$$

where p_i is the nominal position and q_i is its reconstruction from the scalar observation. The model uses outward normals and a positive residual for displacement away from the pivot. The sign needs to be checked on a known displacement when importing a new CALYPSO routine. At one position only the radial projection of the local displacement is available. Tangential components belong to its null space. A sequence of varying normals can identify a restricted geometric model, as developed in Section 4.

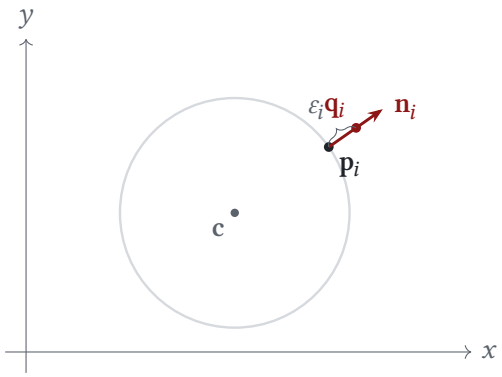

Figure 1.4 – Original definition of the nominal point, reconstructed point and radial deviation [2].

1.4 Planar and spherical trajectory

Write θ for azimuth, φ for elevation above the plane and $\Delta\theta = 2\pi/N$. With $i = 0, \ldots, N-1$ the planar stations occur at $\theta_i = \theta_0 + i\Delta\theta$. Their normals are $(\cos\theta_i, \sin\theta_i, 0)^T$. The same construction in three dimensions is

$$\begin{aligned} n_x &= \cos\phi\cos\theta, \quad n_y = \cos\phi\sin\theta, \\ n_z &= \sin\phi, \quad \rho(\phi) = R\cos\phi, \\ z - c_z &= R\sin\phi. \end{aligned} \tag{1.2}$$

The nominal ten ring centres are at −45°, −35°, …, +45°. There is no equatorial ring in this even-sized spatial grid. The independent planar test supplies the equator. At the extrema, $|z - c_z|$ and ρ both equal $R/\sqrt{2}$, or 106.77 mm for the selected arm. The equal numerical values arise from the 45° envelope and play different geometric roles. The archived displays of generated points and normals use larger plotting scales and show the geometry, not the dimensions of the 151 mm measurement run.

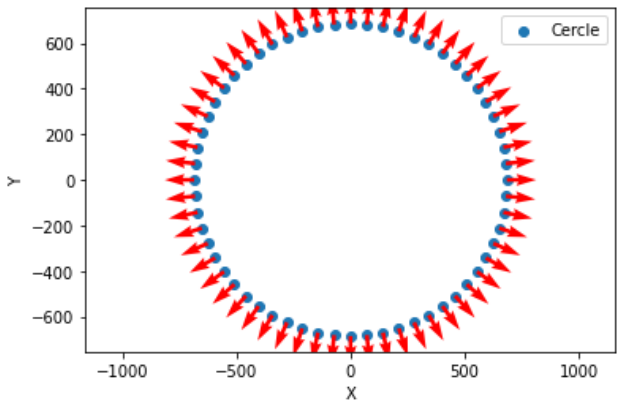

Figure 1.5 – Original computed circle and radial arrows. Axes and the French label « Cercle » are retained. This is a trajectory illustration [1, 2].

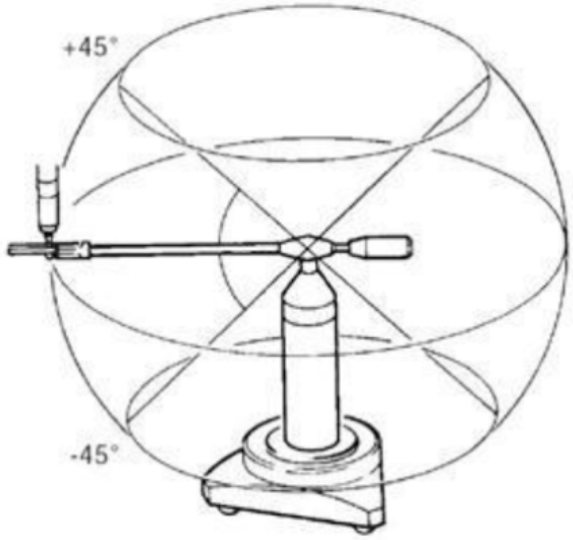

Figure 1.6 – Manufacturer’s MCG sweep illustration reproduced by the project [1, 2]. The ±45° labels delimit the working elevation relative to the base.

1.5 Chord travel and fork clearance

The hand sketch in Figure 1.7 motivated the original numerical study. If consecutive stations on one ring are joined by a straight segment, the midpoint is at radial distance ρcos(π/N). In the same plane, the chord length d_c and maximum radial departure s_c of the segment from the continuous arc are

$$d_c = 2\rho\sin(\pi/N), \qquad s_c = \rho[1-\cos(\pi/N)]. \tag{1.3}$$

Only the contact stations are used for the form measurements. The sagitta describes the path between them under the straight-segment hypothesis. It can be much larger than the micrometre-scale departures at the stations. For a limit d_{max} on the chord, with $0<d_{max}<2\rho$, the exact azimuthal bound is

$$N \geq \max\left(3, \left\lceil \frac{\pi}{\arcsin(d_{\max}/(2\rho))} \right\rceil\right). \tag{1.4}$$

A sagitta limit s_{max} implies the corresponding bound with $\arccos(1-s_{max}/\rho)$ in the denominator for $0<s_{max}<\rho$. Clearance depends on the fork, stylus, probing approach and programmed intermediate motion. The 2024 study selected 60 points after obtaining a preliminary minimum of 30 [1]. The numerical fork clearance and exact controller interpolation were unavailable.

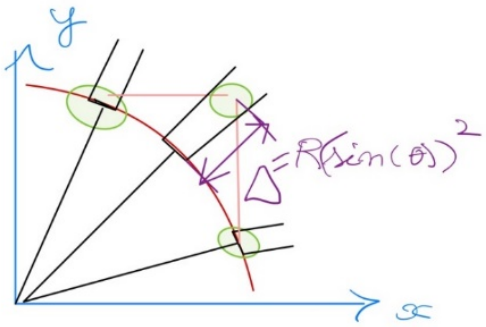

Figure 1.7 – Original hand sketch of the stylus moving between stations. Equation (1.3) specifies the chord and sagitta precisely [1, 2].

Table 1.1 – Equatorial travel geometry for a 151 mm arm. The last row uses a 10° meridional step.

Step	Angle	Chord (mm)	Sagitta (mm)
30 per turn	12°	31.57	0.827
60 per turn	6°	15.81	0.207
Meridian	10°	26.32	0.575

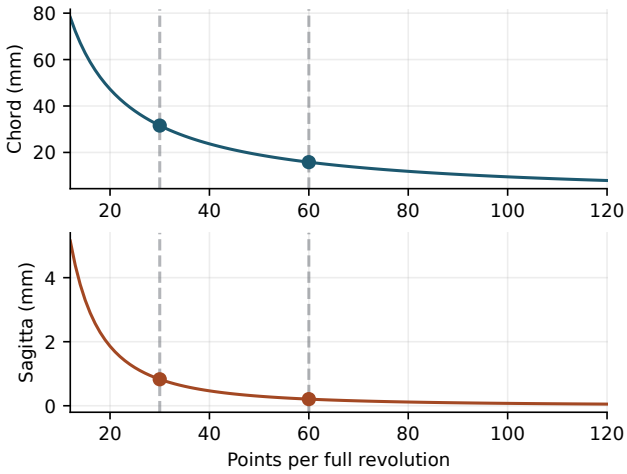

Figure 1.8 – Python calculation for the 151 mm equator. Points mark the archived choices of 30 and 60 samples per turn. The same-azimuth chord between adjacent 10° latitude stations is 26.32 mm.

A fixed azimuthal count reduces the chord at higher elevations. At 45° it is 11.18 mm with 60 stations, compared with 15.81 mm at the equator. Latitude changes require a different movement and clearance check. Connecting two positions at the same azimuth across a 10° change gives a 26.32 mm chord at R=151 mm. A repositioning move between rings may involve a retract and re-approach, which is governed by the actual motion program.

2. Experiment and data reduction

2.1 Generation and CALYPSO input

The trajectories were generated in Python and written for the six arm radii as files with one row per point. Each row contains X,Y,Z,N_X,N_Y,N_Z. The first three entries are positions in a common length unit. The last three are direction cosines. Original code, file listings and an example excerpt appear in Appendix C. The export example has positive Z values because the geometry is represented in the chosen machine frame. For a fit using a local pivot, its coordinates must either be subtracted or carried as part of the model.

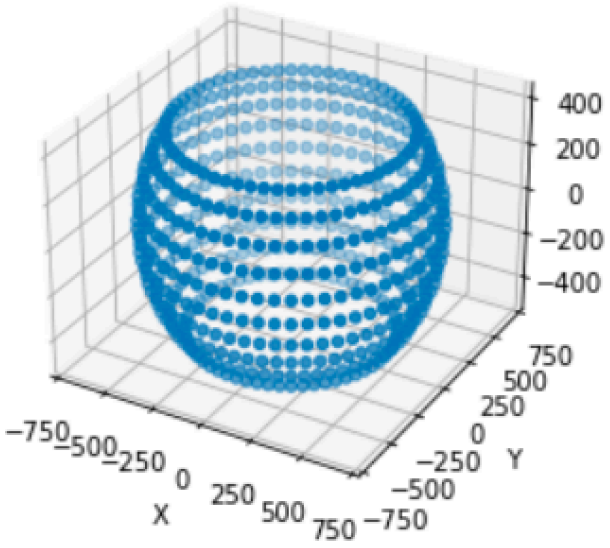

Figure 2.1 – Original plot of nominal stations on the spherical segment [1, 2].

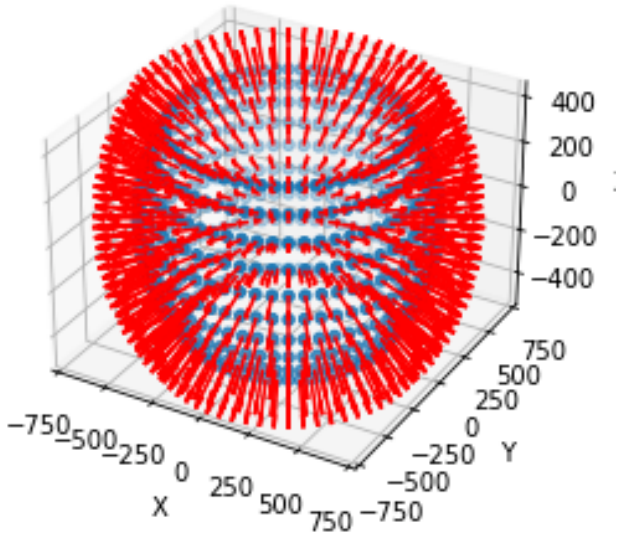

Figure 2.2 – Original plot of the outward direction vectors at spatial contact stations [1, 2].

For a new dataset, validation should address finite coordinates, $\|n_i\|=1$, the expected nominal radius, point and ring counts and traversal order. If rounding coordinates to seven decimal places in millimetres, a nominal row has at most 0.05 nm component quantisation. Unit-normal components rounded to the same decimal precision can produce a norm discrepancy up to 8.7×10^{-8}. Those bounds concern text encoding only. Use persistent station IDs to match a measured row to its nominal row. Revisited stations are intentional in multi-revolution tests.

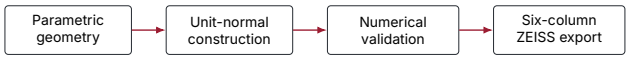

Figure 2.3 – Original workflow for generating and validating nominal rows before export [2].



Figure 2.4 – Original workflow from point data to the scalar residual record [2].

2.2 Planar and spatial sequence design

The planned planar tests included two revolutions in only one direction (positive and negative separately), one revolution in each direction and two in each direction. The CALYPSO names in Table 3.1 preserve the sign order displayed in the images. The original prose sometimes narrates the opposite order. The total revolution counts and whether the path included a reversal can be taken from the paired descriptions. Start direction, exact reversal sample and any repeated endpoint are unresolved without the acquisition file.

For the spatial test, Figure 2.5 records 60 stations in each azimuthal sense at each ring and a complete pass in each vertical order. Taken literally this is 60×2×10×2=2400 nominal visits, or 600 per direction and height-order combination. The dashed and solid paths in the sketch indicate intended ordering. The executed point count and index assignment are unverified. The four estimates printed in the project report correspond to the four labelled combinations.

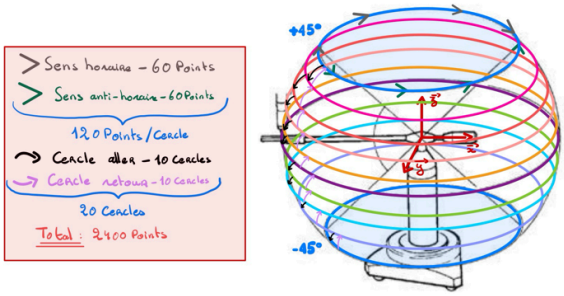

Figure 2.5 – 2024 measurement schedule. CW and CCW scans of each ring were planned for top-down and bottom-up traversals [1, 2].

2.3 Association and comparable endpoints

For a least-squares circle with centre $\hat{c}$ and radius $\hat{R}$, the circle fit is of the radial distances to the planar centre:

$$\begin{aligned}(\hat{\mathbf{c}},\hat{R}) &= \\ \arg\min_{\mathbf{c},R}\sum_i (d_i-R)^2,& \\ d_i &= \|\mathbf{q}_i-\mathbf{c}\|_2, \\ r_i &= d_i(\hat{\mathbf{c}})-\hat{R}.\end{aligned} \tag{2.1}$$

An associated-circle range is max r_i−min r_i. For fixed centre the fitted radius cancels. A minimum-zone deviation minimises that same range over the centre:

$$t_{\mathrm{MZ}} = \min_{\mathbf{c}} \left[\max_i d_i - \min_i d_i\right]. \tag{2.2}$$

The circularity zone uses a planar centre and the sphericity zone uses a three-dimensional centre. Their geometric meaning follows the ISO form-tolerance framework [6]. Ordinary least squares minimises a sum of squares and minimum zone minimises an extreme range, so distinct reported results are possible on a common cloud. The CALYPSO screenshots show the results of the software's circularity evaluation. Evaluation and filter settings cannot be recovered from these screens. Consequently the term "reported circularity" here refers to the printed values and the range used in the synthetic experiment is named separately.

2.4 Reference temperature and uncertainty

A measurement result $Y=f(X_1,\ldots,X_m)$ can depend on artefact geometry, kinematics, probe qualification, temperature and association. For small fluctuations, the GUM gives a first-order propagation with the vector of sensitivities g, input covariance Σ_X and coverage factor k [7]. This preserves covariance terms such as those coupling repeated observations in one ring.

$$\begin{aligned} g_j &= \frac{\partial f}{\partial X_j}, \\ u_c^2(Y) &= \mathbf{g}^T \Sigma_X \mathbf{g}, \\ U &= k u_c. \end{aligned} \tag{2.3}$$

The reference temperature for dimensional properties is 20 °C [8]. For an illustrative arm with α_L=11.5 µm/(m·K), the change is

$$\Delta R_T = \alpha_L R (T - 20\,^{\circ}\mathrm{C}). \tag{2.4}$$

This is 1.74 µm/K at 151 mm. A spatially uniform temperature difference that is constant within a run shifts an ideal arm radius and is absorbed by the fitted constant. Time-varying temperature, gradients or temperature effects on the machine axes can produce angular structure. A numerical uncertainty for the archived circularity or squareness would require calibration records, temperatures, fit and filter settings and repeated runs.

Table 2.1 – Uncertainty mechanisms and experimental checks for a new campaign.

Source	Record or independent check
CMM and probe	Calibration state, stylus ID and qualification, approach direction, repeated contact.
Artefact	Arm certificate, contact condition, repeat mounting and pivot qualification.
Thermal and drift	Machine and arm temperatures, equilibration, intra-run timestamps.
Repeatability	Repeated identically configured paths, analysed at run level.
Association	Fit criterion, filter, sampled angles, data rejection and software version.

3. Planar measurements and direction history

3.1 The four original traces

Figures 3.1–3.4 reproduce all four original CALYPSO plots at one-column width. The red reference and blue trace share a radial amplification of 10,000. At this scale, the shape and separation of lobes can be examined, but their pixel radii cannot be interpreted as machine coordinates. The circularity, point count and stylus field are transcribed in Table 3.1 to allow direct comparison at printed precision.

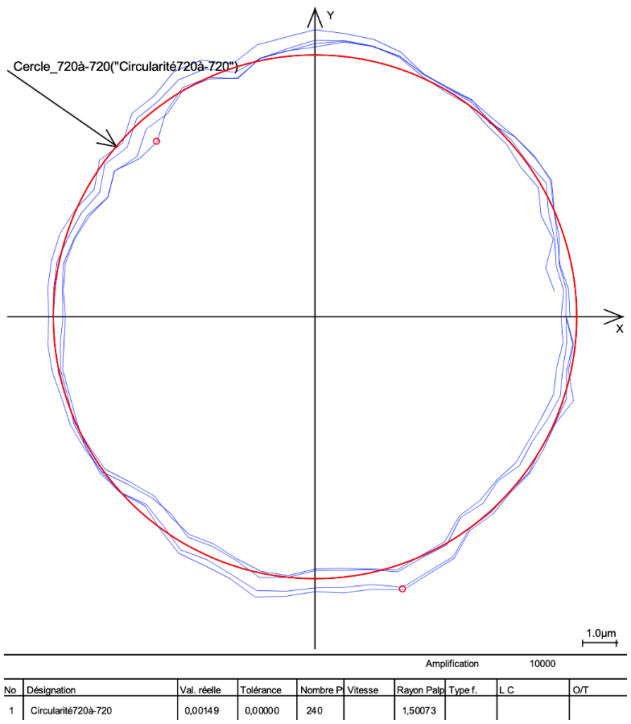

Figure 3.1 – Cercle_720à-720. Four revolutions, described as two in each direction. Reported circularity 1.49 µm from 240 points [1, 2].

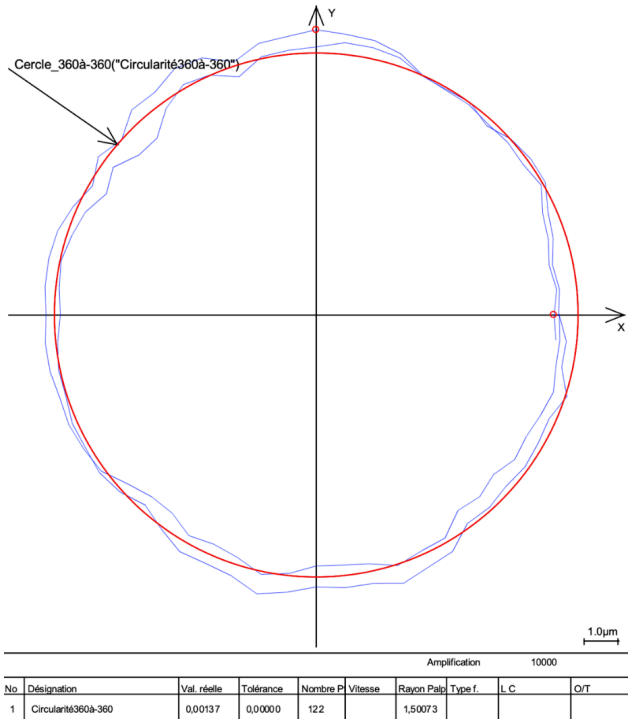

Figure 3.2 – Cercle_360à-360. One revolution in each direction. Reported circularity 1.37 µm from 122 points [1, 2].

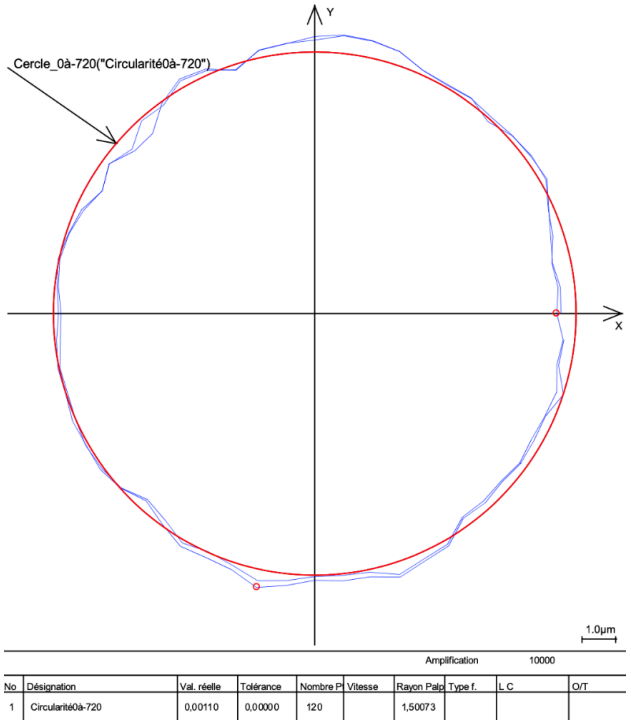

Figure 3.3 – Cercle_0à-720. Two negative-direction revolutions. Reported circularity 1.10 µm from 120 points [1, 2].

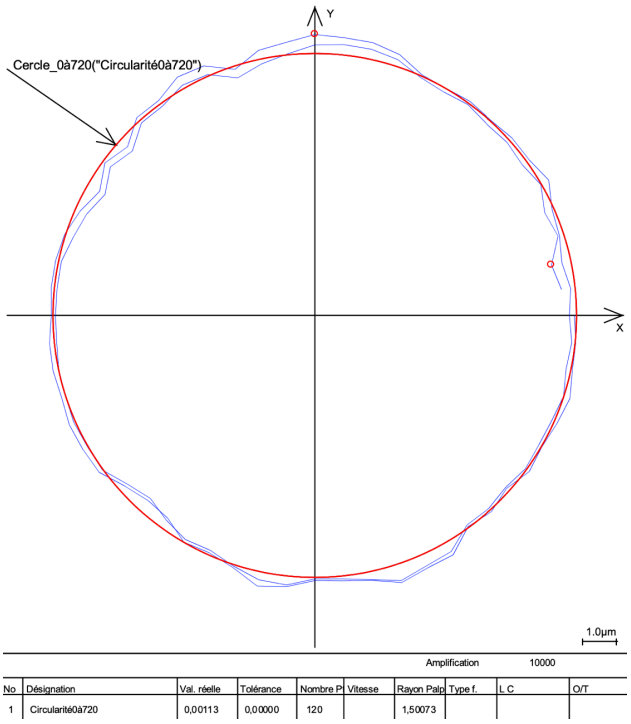

Figure 3.4 – Cercle_0à720. Two positive-direction revolutions. Reported circularity 1.13 µm from 120 points [1, 2].

The 240-point path has the largest reported value. In the polar view, multiple blue arcs are most visible on the lower half and near the positive X direction.

That spread can contain differences between revolutions, reversal transients or acquisition noise. The view has no chronological labels to assign the arcs to a direction. A full four-turn sequence also provides more points and more time for drift than either single-direction path.

The 122-point path has a total number of revolutions comparable to the two single-direction tests. Relative to their 120 samples, the additional two exported points deserve inspection in the raw sequence. The plot shows separations near the lower half and positive X at an intermediate magnitude in Table 3.1. Relative to the two 120-point outcomes the gaps are 0.27 and 0.24 µm. They are compatible with a reversal effect and also with a run-specific change in drift, approach or noise.

The negative- and positive-direction plots share a prominent upper arc above the reference and a smaller-looking width than the two reversal plots. They still show angularly local departures. This suggests examining repeated angular harmonics on a matched grid. The difference of 0.03 µm is a comparison of two ranges. The underlying radial curves could differ at many stations and still yield similar ranges.

Table 3.1 – Numbers transcribed from the four CALYPSO displays. The label ‘Rayon Palp.’ belongs to the stylus field.

CALYPSO designation	Points	Circularity (µm)	Rayon Palp. (mm)	History
Cercle_720à-720	240	1.49	1.50073	reversal
Cercle_360à-360	122	1.37	1.50073	reversal
Cercle_0à-720	120	1.10	1.50073	single direction
Cercle_0à720	120	1.13	1.50073	single direction

3.2 Field labels and descriptive comparison

In every screenshot the value 1.50073 is displayed under *Rayon Palp.*, the probe-radius field. The French report called this a radius and the English version described it as a fitted radius. The field label resolves the discrepancy with the 151 mm arm value: the archive shows a stylus-radius entry. The associated radius of the measured path is unavailable in the printouts. The tolerance field displays 0.00000. A dimensional limit and a decision rule cannot be inferred from that field. Meaningful acceptance or rejection requires a defined limit, comparable evaluation conditions and uncertainty [9].

The two reversal results have an arithmetic mean of 1.430 µm, and the two single-direction results average 1.115 µm. The difference is 0.315 µm, equivalent to 22.0% relative to the reversal mean. Across the four different protocols the sample standard deviation is 0.189 µm. Repetition at identical settings is needed to estimate repeatability. In particular, the four values do not supply a variance estimate for a test of a reversal effect. There is no basis here for a confidence interval on the two-protocol mean difference.

3.3 Sensitivity of an extreme range to sample count

Even for unchanged shape and independent noise, a maximum and minimum depend on how many points were acquired. To quantify the mechanism, the Python experiment uses a shared 60-station angular grid and a static three-harmonic shape in micrometres. At 122 samples the first two stations occur once more in the generated order. A constant and the first azimuthal harmonic are removed by linear least squares to approximate an associated-circle residual.

$$f(\theta) = 0.45\cos(2\theta) + 0.13\sin(5\theta) + 0.07\cos(9\theta). \tag{3.1}$$

Add independent Gaussian noise of 0.12 µm standard deviation, with no direction difference, and run 1600 trials per point count. Table 3.2 and Figure 3.5 give conditional distributions of the resulting extreme range. They are independent of the measured point deviations. The median rises by

0.082 µm between 120 and 240 points, and by 0.007 µm between 120 and 122. At the same time, the central 90% intervals overlap. These magnitudes depend on the selected harmonics, noise distribution and association. They demonstrate a source of confounding in the comparison of unequal runs, and the 122-versus-120 contrast remains a reason to design controlled repetitions.

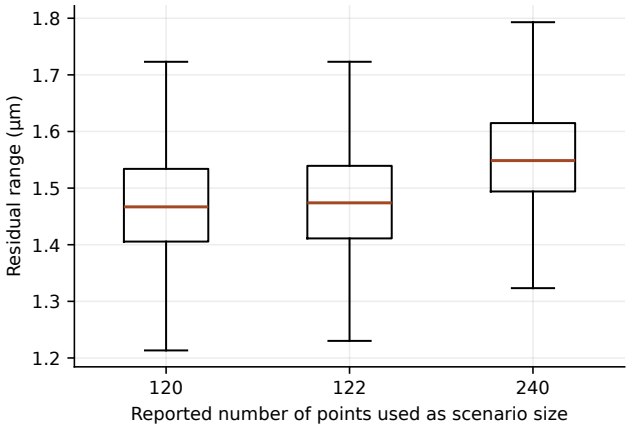

Figure 3.5 – Synthetic range sensitivity with unchanged shape and independent noise. Boxes span the interquartile range. The 122-point scenario adds two revisits to the 120-point grid.

Table 3.2 – Simulated extreme ranges at three observation counts. Values in µm.

Points	Median	5th–95th percentiles
120	1.467	1.324–1.647
122	1.474	1.334–1.643
240	1.549	1.412–1.715

3.4 Paired differences and within-run time

For repeated positions define $h_i=\varepsilon_{+,i}-\varepsilon_{-,i}$ with both directions matched by azimuth and hardware state. Separate the mean, RMS and peak-to-peak quantities:

$$\begin{aligned} \bar{h} &= N^{-1}\sum_i h_i, \\ H_{\mathrm{RMS}} &= \sqrt{N^{-1}\sum_i h_i^2}, \\ H_{\mathrm{pp}} &= \max_i h_i - \min_i h_i . \end{aligned} \tag{3.2}$$

A common reference or consistent joint association is important. Independently zeroing each direction removes a constant contrast from $\bar{h}$. Independent circle fits can additionally remove a first-harmonic contrast. Matching on a nominal grid allows repeatability within each direction to be estimated before a persistent directional difference is interpreted. Time tags for each occurrence preserve the distinction between reversal and drift.

Consider the model $e_s(\theta,t)=f(\theta)+s\,h(\theta)/2+b\,t+\eta$, with $s=+1$ for A and $s=-1$ for B. In ABBA order, at a matched azimuth, define the timing difference Δt between the two direction means:

$$\begin{aligned} \hat{h}_{\mathrm{ABBA}} &= \\ (e_{A1}+e_{A2}-e_{B1}-e_{B2})/2, \\ \Delta t &= (t_{A1}+t_{A2}-t_{B1}-t_{B2})/2, \\ \mathbb{E}[\hat{h}_{\mathrm{ABBA}}] &= h + b\,\Delta t. \end{aligned} \tag{3.3}$$

Equally spaced run starts cancel the start-time part of Δt. For opposite rotations of duration T, a station visited at time τ after an A start is visited approximately at $T-\tau$ after a B start. Then $\Delta t=2\tau-T$ for the ideal schedule. Local timing can still make the estimated directional contrast slope across the circle.

Same-direction differences, A2 minus A1 and B2 minus B1, cancel the fixed shape and direction terms. Fitting these differences against their time separations yields $\hat{b}$. Subtracting $\hat{b}\,\Delta t$ is valid under the stated linear-drift and stationary-shape model. A randomised set of additional blocks and inspection of timestamped residuals would challenge those assumptions. Phase wrapping needs consistent identification of the first point at the seam.

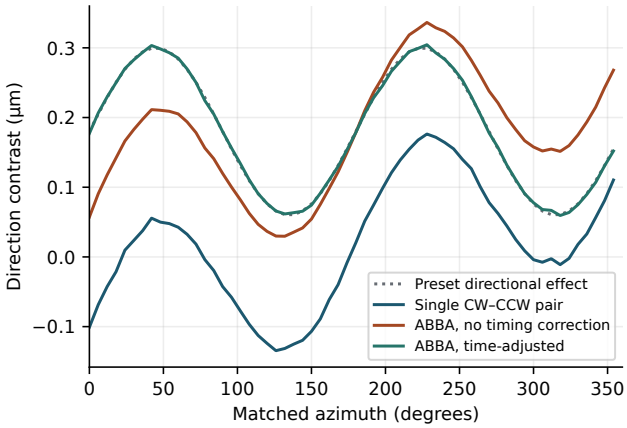

Figure 3.6 – Synthetic ensemble mean contrasts at 60 matched stations. A–B run starts are spaced by 80 s, each turn takes 60 s, residual noise is 0.08 µm and drift is 0.002 µm/s. The dotted curve is the prescribed contrast.

In 1500 synthetic runs, the RMS error relative to the preset directional contrast is 0.209 µm for a single A–B pair, 0.105 µm for the ABBA mean and 0.080 µm after timestamp adjustment. The adjusted result still contains random probing noise. The timing correction is a model test and illustrates the data record needed to decide whether the spatial or planar directions differ systematically.

4. Spatial error identification

4.1 Radius and centre from a radial observation

Let $t=(u,v,w)^{T}$ denote the centre displacement of an idealised realised sphere relative to the reference pivot and let δR be its radius difference. Figure 4.1 shows the original model. Intersect the positive reference ray $(R+\varepsilon_i)n_i$ with the realised sphere. From $\|(R+\varepsilon_i)n_i-t\|^2=(R+\delta R)^2$, the root near R has the form

$$\begin{aligned} a &= R+\delta R, \quad d_i = \mathbf{t}\cdot\mathbf{n}_i, \\ Q_i &= \|\mathbf{t}\|_2^2 - d_i^2, \\ \varepsilon_i &= d_i + \sqrt{a^2-Q_i} - R. \end{aligned} \tag{4.1}$$

Here Q_i is the square of the transverse translation. Rationalising the difference of the square root and a gives

$$\begin{aligned} \varepsilon_i &= d_i + \delta R \\ &\quad - \frac{Q_i}{a+\sqrt{a^2-Q_i}}. \end{aligned} \tag{4.2}$$

The first-order expression is $\varepsilon_i=u\,n_{x,i}+v\,n_{y,i}+w\,n_{z,i}+\delta R$. The omitted geometric term begins at $-Q_i/(2a)$. For the source perturbation (10,20,30) µm and $\delta R=100$ µm its maximum magnitude is bounded by 0.00464 µm at R=151 mm.

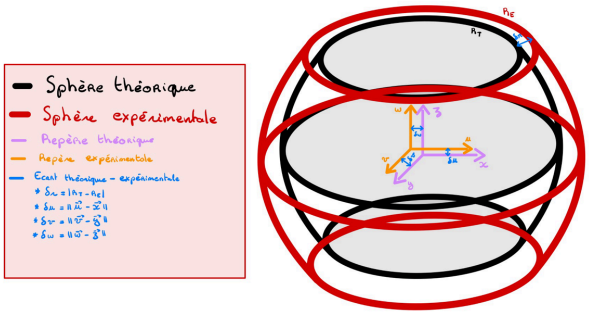

Figure 4.1 – Reference sphere and translated, radius-offset sphere drawn for the 2024 study. The drawing uses exaggerated displacements for clarity [1, 2].

The first-order system uses the translation and radius columns $T_i=(n_{x,i},n_{y,i},n_{z,i},1)$. Denote the observation noise and omitted geometry by η_i. With T^{+} the Moore–Penrose pseudoinverse and full column rank for the second formula, the solution is

$$\begin{aligned} \boldsymbol{\varepsilon} &= T(u,v,w,\delta R)^{T} + \boldsymbol{\eta}, \\ \hat{\mathbf{t}}_4 &= T^{+}\boldsymbol{\varepsilon} \\ &= (T^{T}T)^{-1}T^{T}\boldsymbol{\varepsilon}. \end{aligned} \tag{4.3}$$

The objective is to minimise the sum of squared residuals. The residual at each point may remain nonzero even when the optimum is unique. The four-parameter Python code shown in Appendix C calls a least-squares routine, consistent with the pseudoinverse form. Directly forming the normal equations squares the spectral condition number.

SVD or a rank-revealing QR factorisation is suitable for fitting and auditing a new run.

4.2 Sign convention for small squareness

Write x_i,y_i,z_i for nominal coordinates relative to the local pivot. The legacy angular columns arise from a displacement with Y component $-\alpha\, z_i$, Z component $-\beta\, x_i$ and X component $-\gamma\, y_i$. Their normal projection gives

$$\begin{aligned} \varepsilon_i \simeq \mathbf{n}_i^T \mathbf{t} + \delta R \\ -\alpha z_i n_{y,i} - \beta x_i n_{z,i} \\ -\gamma y_i n_{x,i} + \eta_i. \end{aligned} \tag{4.4}$$

The coefficients correspond to YZ, XZ and XY, respectively, under these shear signs. The French source labels both β and γ as XY in the prose. The equations and the legacy implementation place β in XZ. Departures from this convention, including the sign of the residual, change the interpretation of the angles.

For a general small affine error K, the radial signal is $R\, n^T K n$. Decompose $K=S+W$ with $S=(K+K^T)/2$ and $W=(K-K^T)/2$. The skew part satisfies $n^T W n=0$, since its transpose is the negative of itself. An infinitesimal rigid rotation of an ideal sphere produces no radial signature. A common scale error sI enters as Rs and is exactly confounded with a radius offset at one R. Directional scale and straightness, probe lobing and mounting effects can alias or appear in residuals. The fitted angular quantities are coefficients of this restricted field.

Using absolute coordinates with the same signs also changes translation terms. With $z_i^{abs}=z_i+c_z$, the α contribution contains an extra $-\alpha\, c_z\, n_y$, collinear with $v\, n_y$. The β and γ terms have analogous couplings. Outer-loop paths at different placements should therefore be compared in a defined coordinate frame, including how local centres are qualified.

4.3 Scaling, joint solution and staged projection

On a nominal sphere, $x_i=Rn_{x,i}$, and similarly for Y and Z. Use b in units of length and a dimensionless row X_i:

$$\begin{aligned} \mathbf{b} = (u, v, w, \delta R, R\alpha, R\beta, R\gamma)^T, \\ \mathbf{X}_i = (n_x, n_y, n_z, 1, \\ -n_y n_z,\ -n_x n_z,\ -n_x n_y). \end{aligned} \tag{4.5}$$

The forward relation is $\varepsilon=Xb+\eta$. When residuals are in µm, use R=151000 µm. A 1 µrad angle represents a 0.151 µm coefficient before multiplication by the normal product. Numerical column equilibration in the English source uses $D_{jj}=\|A_{:j}\|_2$ and $\tilde{A}=AD^{-1}$ when every column has nonzero norm. Its solution is $\hat{q}=D^{-1}\tilde{A}^{+}\varepsilon$ when the model has full rank. The condition numbers below use X with the common physical scale so they are comparable across grids.



Figure 4.2 – Original schematic of the proposed joint fitting workflow [2]. Column scaling, solver and residual diagnostics are recorded as separate operations.

Partition X=[T S] where S contains the three angular columns. The original staged method fits T first and regresses the residual independently on each column of S. To see the assumptions, eliminate the four nuisance coefficients using the orthogonal projector $P_T=TT^{+}$:

$$\begin{aligned} M_T = I - P_T, \\ \hat{\mathbf{b}}_S = (M_T S)^{+} M_T \boldsymbol{\varepsilon}, \\ \hat{\mathbf{b}}_T = T^{+}(\boldsymbol{\varepsilon} \\ -S\hat{\mathbf{b}}_S). \end{aligned} \tag{4.6}$$

The joint expression follows by minimising $\|M_T(\varepsilon-Sb_S)\|^2$. It reduces to the legacy stage-by-stage expressions with unadjusted denominator $S_j^T S_j$ when $T^T S=0$ and the columns of S are mutually orthogonal. Symmetric complete azimuth and elevation sampling produces these orthogonalities for centred spherical geometry. Missing azimuth sectors, asymmetric filtering or an absolute coordinate offset can break them.

4.4 Reading rank and singular values

For a full azimuth sweep, the averages of the odd harmonics vanish and the means of $\cos^2\theta$, $\sin^2\theta$ and

$\cos^2\theta\sin^2\theta$ are 1/2,1/2,1/8. With a symmetric distribution in $s=\sin\varphi$, define $m_2=E[s^2]$ and $m_4=E[s^4]$. Averaging n_y^2 $n_z^2=(1-s^2)s^2\sin^2\theta$ yields $(m_2-m_4)/2$, and averaging n_x^2 n_y^2 yields $(1-2m_2+m_4)/8$. The cross terms vanish by azimuthal and vertical symmetry. For equally weighted observations per station,

$$\begin{aligned} \frac{X^{T}X}{N} &= \operatorname{diag}(d,d,m_2,1,e,e,f),\\ d=(1-m_2)/2,\qquad & e=(m_2-m_4)/2,\\ f=(1-2m_2+m_4)/8.& \end{aligned} \tag{4.7}$$

An equator-only test gives $n_z=0$, so w,α,β are unidentifiable and the rank is four. On one off-equator ring, n_z is constant and the vertical translation is confounded with radius. There the two z-related shear columns are proportional to Y and X translation columns. The rank is still four at +45°. The 10-ring design has full rank in the synthetic centred geometry, with singular values divided by √600 of approximately 1.000, 0.626, 0.626, 0.465, 0.284, 0.262 and 0.262. Its condition number is 3.81. This quantifies the availability of model directions at the nominal stations. It provides no independent control of scale, artefact or drift.

4.5 Coefficient uncertainty and robust estimation

For fit rank p and iid residuals, the usual residual variance and covariance estimates are

$$\begin{aligned} \hat{\mathbf{r}} &= \boldsymbol{\varepsilon} - X\hat{\mathbf{b}},\\ \hat{\sigma}^2 &= \frac{\|\hat{\mathbf{r}}\|_2^2}{N-p},\\ \operatorname{Cov}(\hat{\mathbf{b}}) &\simeq \\ \hat{\sigma}^2 &(X^{T}X)^{-1}. \end{aligned} \tag{4.8}$$

If additive random effects couple stations within rings, set $Z_{ij}=1$ for a station i in ring j and zero elsewhere. Independent white noise of variance σ^2 and independent ring offsets of variance τ^2 give

$$\begin{aligned} \Sigma &= \sigma^2 I + \tau^2 Z Z^{T},\\ \operatorname{Cov}(\hat{\mathbf{b}}) &= X^{+}\Sigma (X^{+})^{T}. \end{aligned} \tag{4.9}$$

The model calculation below uses σ = 0.15 µm and τ = 0.30 µm. In a complete azimuth sweep, a common ring offset is orthogonal to all terms with azimuthal oscillation. The uncertainty therefore enters effective radius and vertical translation preferentially. At those settings their standard errors increase from 0.006 to 0.095 µm and from 0.013 to 0.204 µm, respectively. Treating correlated rows as 600 independent points would underestimate these uncertainties. They are modelled examples, with no σ or τ estimated from archived data.

Table 4.1 – Predicted OLS coefficient standard errors for independent noise, and with an additional common random offset per ring.

Term	Unit	Independent	Ring offsets
u	µm	0.010	0.010
v	µm	0.010	0.010
w	µm	0.013	0.204
δR	µm	0.006	0.095
α	µrad	0.155	0.155
β	µrad	0.155	0.155
γ	µrad	0.143	0.143

Huber weights limit the influence of large residuals in regression [10]. The implemented iteratively reweighted scheme uses the median absolute deviation of residuals as a scale estimate and c=1.345. For scale $\hat{s}>0$, it applies

$$\begin{aligned} u_i = r_i/\hat{s},\quad & w_i = \min(1, c/|u_i|),\\ \hat{\mathbf{b}}_{\mathrm{new}} &= \\ \arg\min_{\mathbf{b}} &\| W^{1/2}(X\mathbf{b} \\ &-\boldsymbol{\varepsilon})\|_2^2. \end{aligned} \tag{4.10}$$

At $u_i=0$ take $w_i=1$. This is a diagnostic fit. With 12 isolated spikes of magnitude 1.5 µm and white noise σ = 0.15 µm on the nominal grid, 200 seeded trials give median coefficient RMS errors of 0.028 µm for OLS and 0.017 µm for Huber. The corresponding 90th percentiles are 0.042 and 0.025 µm. The errors are computed in the scaled b units. This experiment tests sparse spikes of known magnitude. A coherent lobe, repeated offset or high-leverage point may behave differently. For inference under heteroscedasticity or correlation, use covariance propagation or run-level resampling with adequate independent runs.

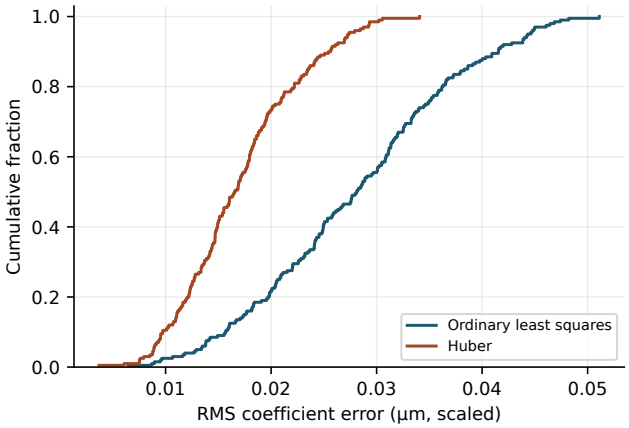

Figure 4.3 – Synthetic distributions of scaled coefficient RMS error for 200 trials with 12 isolated additive spikes per trial.

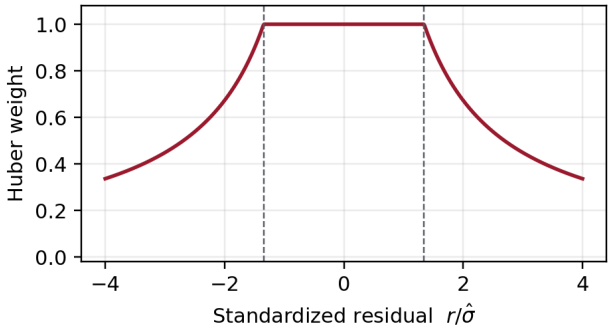

Figure 4.4 – Original illustration of the Huber residual weight law from [2]. Unit weight is used in the central interval.

5. Audit of the archived spatial estimates

5.1 The original recovery experiment

The 2024 test prescribed centre offsets of 0.010, 0.020 and 0.030 mm, a radius difference of 0.100 mm, and angles of 0.1, 5 and 10 µrad. Table 5.1 preserves the values with lengths converted to µm. The model recovered δR and w at reported precision and came within 0.033 µm on u. The estimates of α and β were 98.79 and 9.88 times their inputs. The γ estimate was within rounding of the prescribed 10 µrad. This mixed result must be qualified by parameter.

Table 5.1 – Input and legacy recovered values from the 2024 synthetic example [1].

Term	Unit	Input	Recovered
δR	µm	100.0000	100.00000
u	µm	10.0000	9.96725
v	µm	20.0000	19.99935
w	µm	30.0000	30.00000
α	µrad	0.1000	9.87938
β	µrad	5.0000	49.38692
γ	µrad	10.0000	9.99999

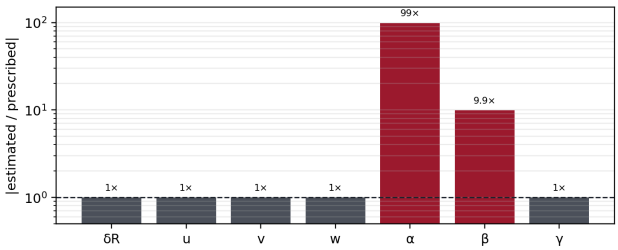

Figure 5.1 – Recovery errors plotted in the English project report [2]. The graph summarizes the 2024 synthetic fit, not the new Python trials.

A scale-sensitive metric can supplement absolute error. The original study defines $e_j=\hat{q_j}-q_j$ and $E_j=|e_j|/\max(|q_j|,q_{j,\min})$ with a stated positive floor. A zero-valued channel needs an absolute tolerance in the same units. The angular outputs in Table 5.1 are many times larger than possible quantisation in the exported text at seven decimal places in mm.

5.2 What the recovered code establishes

Appendix C shows the original generator function `cootest` and its importer. The first increasing-azimuth loop in the top-down half uses only $u\,n_x+v\,n_y+w\,n_z+\delta R$. Each of the other three loops includes the three signed shear terms of Eq. (4.4). Thus the use of the generator for a full angular test depends on which branch is selected. The listing also constructs its coordinates using R plus the prescribed radius difference. For the 0.100 mm case, that change amounts to 0.066% of the nominal radius and sets the scale of this particular convention change. The importer uses integer division of a zero-based row by 60, parity selection and a half-file split. Such a parser requires identical block counts and cannot infer the direction name from the coordinates alone. In particular, the exact parity used to produce each legacy table row, the input file contents and the software run configuration were not available.

In a balanced synthetic test, the branch that omits the angular terms gives zero in those three fitted channels. Combining one omitted branch with three correct branches of equal size gives 0.75 of each prescribed angle. Those counterfactuals establish the effect of the omission under a controlled geometry. They cannot generate the simultaneous 98.79 and 9.88 amplification in the archived table. Fitting each angular term after a separate translation step and using uncentred coordinates are additional mechanisms for cross-talk. The exact source of the archived magnitudes remains open.

5.3 Independent tests of the estimator

The first replay injects all seven linear terms with the same definition on every path. A seven-column basis test checks signs and scales. The nominal fit is then evaluated on a separate angular grid with equal-area rings and a half-step azimuth phase. The maximum discrepancy is below 10^{-12} µm in double precision. This is an implementation identity and checks only the linear forward model. The next replay uses the exact translated-sphere root in Eq. (4.2), plus the three linear shears. The maximum radial difference is 0.00463 µm, with cross-term estimates shifted by −0.0263, −0.0131 and −0.0088 µrad. The estimate of α is sensitive in relative terms because its prescribed magnitude is just 0.1 µrad.

A further test treats the sphere as an affine shape before ray intersection. With the matrix $M=I+K$ built from the three signed shears, let $v=M^{-1}n$ and $w=M^{-1}(Rn-t)$. Then $A=v^Tv$, $B=v^Tw$ and $C=w^Tw-(R+\delta R)^2$ give the exact intersection residual near the nominal radius:

$$A\varepsilon^2+2B\varepsilon+C=0,\qquad \varepsilon=\frac{-C}{B+\sqrt{B^2-AC}}. \tag{5.1}$$

Table 5.2 lists the coefficients and the maximum pointwise difference from the first-order model. These tests only validate the geometry and solver within the prescribed perturbations. They use no calibration measurements.

Table 5.2 – Bias of the linear fit in two independent geometric simulations. Final row is the maximum difference between each generated radial field and the first-order field.

Term	Unit	Translated root + shear	Affine shape
u	µm	0.00000	0.00021
v	µm	0.00000	0.00006
w	µm	0.00000	0.00002
δR	µm	−0.00334	−0.00334
α	µrad	−0.02630	−0.02621
β	µrad	−0.01315	−0.00984
γ	µrad	−0.00877	−0.00214
Max radial Δ	µm	0.00463	0.00505

For an incomplete example, keep $n_x > -0.55$ and on the two lowest rings retain only $n_y > 0$. The resulting 387 rows have condition number 5.84. The joint fit recovers the noiseless prescribed angles. With staged estimation the three angles are −0.514, 2.430 and 8.701 µrad. Even if all four sign and order groups are collected, these deviations can arise whenever data loss breaks the symmetry of a group fitted separately. The observable rank alone does not protect a staged estimator.

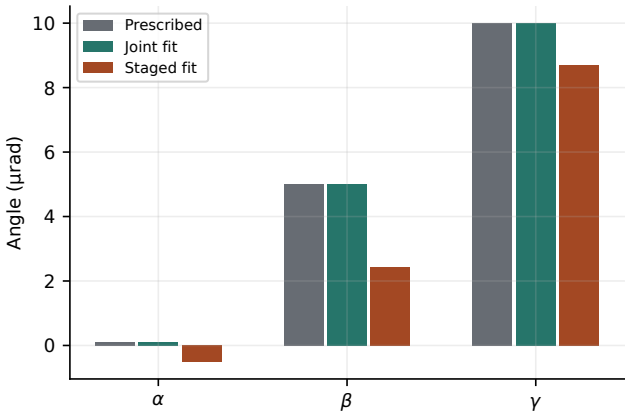

Figure 5.2 – Synthetic test of joint and staged fits with 387 retained stations and no random noise. The original perturbation is used, while the missing-sector rule is illustrative.

At an illustrative coordinate offset $c_z = 40$ mm, with full sampling and the uncentred α column, a staged fit returns 0.0714 µrad for a prescribed 0.1000 µrad. A joint fit on the same design recovers 0.1000 µrad. Re-centring the design while retaining the data generated with the absolute-coordinate model shifts the fitted v by −0.0040 µm, consistent with the term $-\alpha\, c_z$. The offset used here was chosen for the demonstration. The original experiment does not supply a verified offset for such a replay.

5.4 The four reported fits to CMM records

Table 5.3 gives all printed spatial estimates from [1]. The centre and radius magnitudes are sub-micrometric. The spread in w across protocols is 0.539 µm. α ranges from −1.400 to +3.413 µrad, while γ ranges from −1.543 to +2.064 µrad. For the bottom-up order, α changes sign between directions, and both bottom-up w values are positive while both top-down values are negative. The source therefore records a substantial dependence on how the dataset was partitioned.

Table 5.3 – Reported coefficients computed from the CMM acquisitions [1]. Units are converted from mm and rad. Entries are printed to three decimals.

Path	δR (µm)	u (µm)	v (µm)	w (µm)	α (µrad)	β (µrad)	γ (µrad)
CW top-down	0.026	0.159	−0.033	−0.087	−0.783	−0.312	0.265
CCW top-down	−0.001	0.174	0.039	−0.180	−1.400	0.490	1.485
CW bottom-up	−0.123	−0.133	−0.033	0.359	−0.797	−0.103	2.064
CCW bottom-up	−0.074	−0.198	0.062	0.179	3.413	−0.601	−1.543

The arithmetic contrast of the two bottom-up and two top-down w estimates is +0.403 µm. The corresponding contrast between mean CCW and mean CW v is +0.083 µm. These are descriptive contrasts from four results with different path histories. They could arise from real motion history, drift, indexing, association or correlation between terms. No independent spatial repetitions or residual covariance were available to separate them. Even a small residual would leave the distinct calibration, probe and artefact contributions unresolved. The published angular coefficients cannot support a CMM compensation update on this evidence.

6. Coverage, sampling and signal analysis

6.1 Spherical area and missing directions

For p=c+Rn(φ,θ) the cross product of the tangent vectors has norm $R^2\cos\varphi$ within the envelope. With s=sinφ, the area element and integrated zone area are

$$\begin{aligned} \mathrm{d}A &= R^2 \cos\phi \,\mathrm{d}\phi \,\mathrm{d}\theta \\ &= R^2 \,\mathrm{d}s \,\mathrm{d}\theta, \\ A_{\text{zone}} &= 2\pi R^2 (s_2 - s_1). \end{aligned} \tag{6.1}$$

The ±45° band contains a=sin 45°=0.7071 of the surface, or 0.2026 m² for R=151 mm. Each remaining cap has about 14.64% of the reference surface. The ten rings are a finite set of curves and this percentage describes the continuous angular envelope. It does not measure how much of the CMM work volume has been verified. Scaling or translating the same horizontal arrangement can move the sampled points to other locations while retaining the same angular null space.

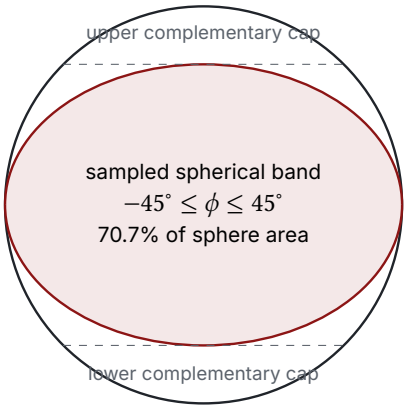

Figure 6.1 – Original schematic of the ±45° belt and polar caps [2]. The percentages refer to the reference sphere surface.

The 2024 report proposes tests at higher and lower regions of the working volume [1]. A useful decomposition is spatial relocation with a vertical base, versus changing the available normal directions. The first needs known placements and overlapping regions. For the second, an idealised comparison uses two perpendicular axes a_1,a_2 for the belts. A unit normal outside both belts would satisfy $|a_1\cdot n|>1/\sqrt{2}$ and $|a_2\cdot n|>1/\sqrt{2}$, whose squared sum would exceed one. Two such ideal belts therefore cover all normal directions. This is a geometric limit only. Alternate artefacts or fixtures must be qualified for orientation, stability and probe

accessibility. The original report gives no results from a tilted MCG, nor any quantitative comparison at −45° with a larger calibrated reference.

6.2 Choice of ring distribution

For M rings and |s|≤ a, equal area follows by dividing s into equal bands, selecting their midpoints and choosing the same count N_θ on each ring:

$$s_j = -a + \frac{2a(j+1/2)}{M}, \quad \phi_j = \arcsin s_j, \qquad A_{\text{cell}} = \frac{4\pi R^2 a}{M N_\theta}. \tag{6.2}$$

Here j=0,…,M−1. Equal area follows from the cell boundaries, with the centres inside them. Putting the first and last ring centres directly on the boundaries gives half-width edge cells if one uses midpoints between rings to assign areas. Multiplying the count by ρ_j/R on equally spaced s-bands instead gives more points per unit area near the equator. It addresses horizontal travel spacing. For equal elevation bands and an approximately fixed azimuthal chord, a ρ_j-proportional count approximates equal-area density away from the end bands.

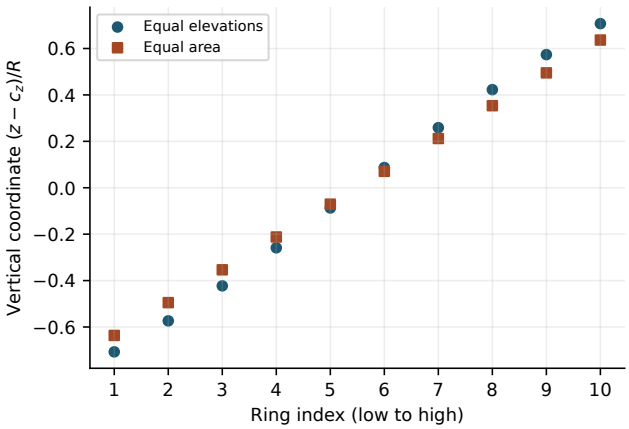

Figure 6.2 – Ring centres in equal-elevation and equal-area designs, each with ten rings. In the latter, the cell boundaries span ±45° and the outer centres are at ±39.52°.

The original spacing prescription uses the ceiling of $2\pi\rho_j/d_t$ with a minimum number of azimuthal points. For positive d_t, the arc between stations is an upper bound on the chord. Equation (1.4) gives the exact chord-based count when the geometric regime applies. Meridional gaps and angular transitions must be inspected separately. For surface coverage and a required shear precision, this need not be the same optimum.

For a uniform belt in s, $m_2=a^2/3$ and $m_4=a^4/5$. Equation (4.7) then gives the continuous-area curve in Figure 6.3. As a tends to zero the weak vertical terms have singular values proportional to a, while w vanishes on the equator. At full sphere the continuous condition number is √15. Around ±45°, greater weight near the boundary of the nominal design helps the n_y n_z and n_x n_z terms. The 600-point Python comparisons give 3.81 for the equi-elevation design, 4.14 for the equal-area rule, and 4.28 when the same equal-area ring locations use circumference-weighted counts. Equal-area sampling serves spatial representativeness. When the priority is a specified coefficient combination, comparing its variance under a common time or point budget provides the relevant criterion.

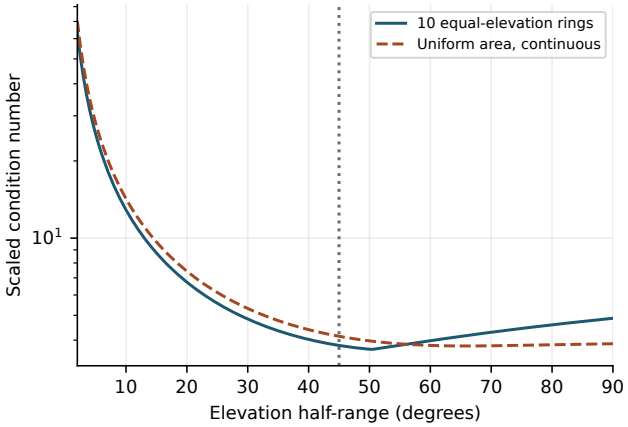

Figure 6.3 – Scale-aware condition number versus elevation half-range. The marker indicates the MCG's nominal 45° limit. Results beyond it are geometric comparisons.

Table 6.1 – Common 600-point budget in the ±45° nominal belt. κ refers to the matrix scaled in Eq. (4.5).

Design	Rank	κ
Equal elevation, 60 per ring	7	3.81
Equal area, 60 per ring	7	4.14
Equal-area rings, variable count	7	4.28

6.3 What the legacy MATLAB routine subtracts

The archived MATLAB listing loads six nominal and six measured columns, subtracts them

componentwise and calculates their five-sample moving averages. It then subtracts those averages from the measured coordinates and normal components. If a field has error $e_i=q_i-p_i$, the output field error is $(I-M_5)e$, where M_5 denotes the moving average. The slowly varying part of the input error is removed and the faster-varying part remains. This distinction is important for periodic verification. Suppressed low angular harmonics can include the artefact or machine signature that the test was intended to monitor.

With a periodic centred window and 60 equally spaced stations per turn, the transfer for harmonic m of the scalar subtraction is

$$\begin{aligned} \omega_m &= 2\pi m/60, \\ G_{\mathrm{sub}}(m) &= 1-\frac{1}{5} \\ &\quad \sum_{j=-2}^{2} \cos(j\omega_m). \end{aligned} \tag{6.3}$$

The archived MATLAB function uses the default endpoint handling, so Eq. (6.3) describes the interior of a regularly sampled uninterrupted series. With a varying normal, componentwise filtering followed by radial projection can have different properties. The listing treats normal components like coordinates and does not renormalise the vectors. Its output is therefore unsuitable as a substitute for nominal unit normals. The original MATLAB code and its screenshot are preserved in Appendix C and as an embedded attachment.

6.4 Hampel and Savitzky–Golay diagnostic view

A Hampel step computes a local median m_k and median absolute deviation scale s_k:

$$\begin{aligned} m_k &= \mathrm{median}_{j\in w_k} e_j, \\ s_k &= 1.4826\,\mathrm{median}_{j\in w_k}|e_j-m_k|. \end{aligned} \tag{6.4}$$

The diagnostic replaces a sample by m_k when $|e_k-m_k|>3s_k$. A false flag can occur near a steep or asymmetric lobe, and clusters of extreme values can raise the local threshold. Savitzky–Golay (SG) filtering uses a cubic least-squares polynomial in the 21-sample local window [11]:

$$\begin{aligned} \hat{\mathbf{a}}_k &= \arg\min_{\mathbf{a}} \\ &\sum_{j=-10}^{10}\left(e_{k+j}-\sum_{p=0}^{3} a_p j^p\right)^2, \\ e_{\mathrm{SG}}[k] &= \hat{a}_{0,k}. \end{aligned} \tag{6.5}$$

On an equidistant periodic grid with c_j the convolution weights, the linear stage has gain $\sum_{j=-10}^{10} c_j \cos(j\omega_m)$. The coefficients sum to unity, preserving DC. At 60 points per turn, the 21-point window spans 120° from first to last station. Its signed gain at order 2 is 0.932, and at order 5 it is −0.009. Thus the smooth curve can retain a two-lobe shape while removing practically all of a five-lobe signal. The subtraction in Eq. (6.3) retains only 0.043 of a second-order lobe. On the fixed circle the operator is symmetric, so negative gains are sign reversals of those harmonics.

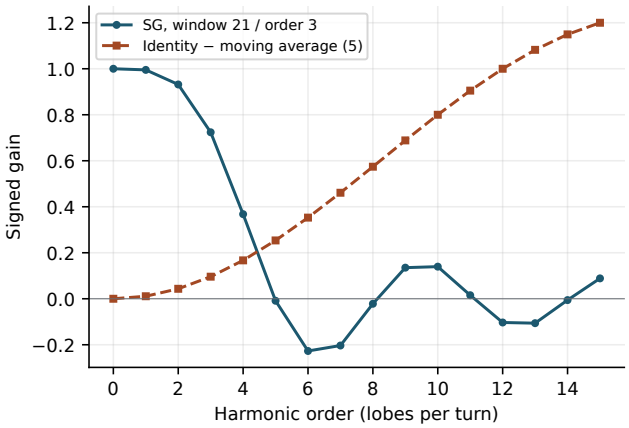

Figure 6.4 – Signed harmonic gains for the periodic scalar calculation at 60 stations per turn. The nonlinear Hampel stage is excluded from this transfer function.

The earlier English report simulated four revolutions with 0.18 µm observation noise and three injected spikes. Figure 6.5 and Table 6.2 preserve its published diagnostics. Full random seed and raw synthetic values were unavailable, so its correlation of 0.988 is retained as reported. The new Python experiment uses a separate 240-point synthetic record with $0.4\cos(2\theta)+0.12\sin(5\theta)$ µm of prescribed form, 0.12 µm white noise and three known spikes. It wraps the window for a fully periodic demonstration and marks nine samples in all. The raw-to-truth RMS is 0.188 µm, the Hampel plus SG value is 0.101 µm, and the boxcar-subtracted RMS is 0.327 µm. The SG RMS

improves while missing part of the actual preset shape. Both angular gain and feature residuals need inspection.

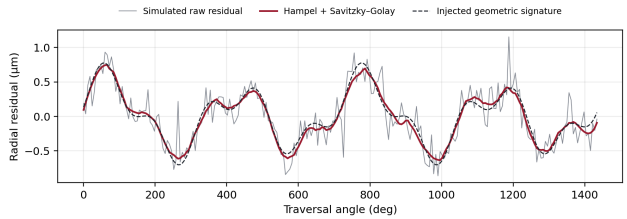

Figure 6.5 – Preserved simulated filtering curves from the English project report [2]. The figure is associated with the historical diagnostic values in Table 6.2.

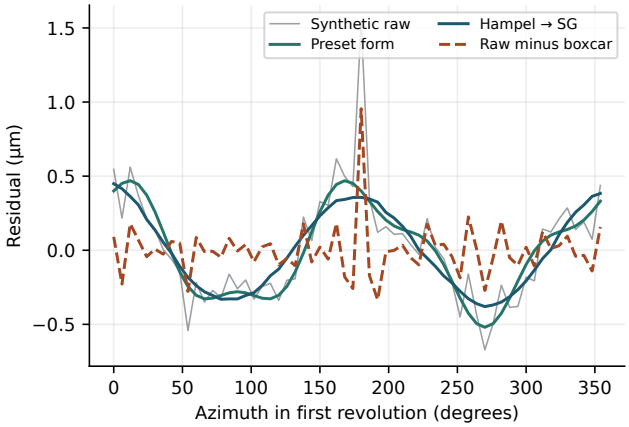

Figure 6.6 – Independent Python simulation with two- and five-lobe form. The plot shows the first of four turns and distinguishes the preset form from three processing views.

Table 6.2 – Diagnostics in the earlier simulated filtering example [2].

Indicator	Raw	After filtering
RMS error (µm)	0.187	0.058
Peak-to-valley (µm)	2.017	1.383
Form correlation	—	0.988

Matched continuous revolutions can be combined in the angular domain for diagnosis. Concatenating opposite directions creates a different ordering, and a periodic filter should not wrap across a reversal or an unrecorded transition. Retain raw deviations, fit and filter metadata, replacement flags and angular grid alongside diagnostic plots. Conformity requires the association and filtering procedure specified for the intended measurand [6, 9].

7. Verification protocol and findings

7.1 Repeatable measurements

The original proposal separates preparation, planar baselines, spatial measurements and trending [1, 2]. The minimum data fields and experimental controls are specified below.

Preparation. Record CMM identity, artefact and stylus serial numbers, calibrations, temperature sensors, machine and artefact temperatures, software version and reference-frame definition. Verify probe qualification and use the same preconditioning path. For each setup, preserve the original radius value, local pivot, axis convention, clearance assumptions and qualification record.

Planar baseline. Collect at least five repeat two-turn runs in each direction at a fixed grid, approach, acquisition settings and speed. Include independent alternating blocks for direction comparisons and a separate series with deliberate reversals. Compare matched angular differences in a common reference, record in-run timing and use a consistent association and acquisition window. Distinguish the between-block mean contrast from within-direction repeatability and within-run drift.

Spatial tests. Preserve the four path-history labels for each point. Repeat each combination with balanced run ordering. Fit jointly in a common coordinate convention and report rank, scaled singular values, residual RMS and residual structure by ring, azimuth, timestamp and direction. Record the units, signs, estimator and flags, and use separately qualified artefact positions and more than one arm length where appropriate. An independent

reference is needed to validate the fitted geometry, especially any angular adjustment.

Trend and decision. Keep the archive of nominal points, raw deviations and operational metadata alongside derived plots and tables. Set monitoring limits from repeat campaigns under known conditions. For a conformity decision, specify the verification measurand and a decision rule incorporating measurement uncertainty [7, 9]. The four available planar captures support a descriptive trend only. See Appendix D for the recommended field schema.

7.2 Conclusions

The 2024 campaign produced four circularity plots with printed values from 1.10 to 1.49 µm. The reversal-containing runs had a higher mean by 0.315 µm. A noise-only simulation shows that unequal sample counts can change an extreme range, and an opposite-direction timing model shows residual bias within a balanced run order. The archived data cannot isolate hysteresis. The CALYPSO field originally interpreted as a path radius is the stylus-radius field.

The centred ten-ring geometry can identify seven scaled coefficients in the restricted model. The original recovery has two large angular discrepancies and an asymmetry in its synthetic generator. Independent tests quantify omission, centring, incomplete sampling and nonlinear effects. They establish conditions for using the estimator and leave the actual experimental angles unvalidated. The 70.7% coverage value is an angular surface fraction. Extending the machine workspace or adding new normal directions requires separate positioning or artefact qualification. All four original polar plots, the original formula material and the code excerpts remain with the manuscript.

References

[1] D. Kumar and T. Ho. *Suivi périodique des MMT. Établir un protocole pour améliorer la couverture spatiale de ma Machine Checking Gauge*. OPM project report, École Nationale Supérieure d’Arts et Métiers, Lille, semester 8, 2024. Unpublished French project record.

[2] D. Kumar and T. Ho. *Spatial Verification of a Coordinate Measuring Machine*. English project report documenting the 2024 work, 31 pp. Unpublished source PDF.

[3] Renishaw plc. *Machine checking gauge (MCG) system user’s guide*, issued December 2021. Renishaw guide.

[4] International Organization for Standardization. ISO 10360-2:2009, *Geometrical product specifications. Acceptance and reverification tests for coordinate measuring machines. Part 2: CMMs used for measuring linear dimensions*. ISO catalogue.

[5] International Organization for Standardization. ISO 10360-5:2020, *Geometrical product specifications. Acceptance and reverification tests for coordinate measuring systems. Part 5: CMMs using single and multiple stylus contacting probing systems*. ISO catalogue.

[6] International Organization for Standardization. ISO 1101:2017, *Geometrical product specifications. Geometrical tolerancing. Tolerances of form, orientation, location and run-out*. ISO catalogue.

[7] Joint Committee for Guides in Metrology. JCGM 100:2008, *Evaluation of measurement data. Guide to the expression of uncertainty in measurement*. BIPM, 2008. 10.59161/JCGM100-2008E.

[8] International Organization for Standardization. ISO 1:2022, *Geometrical product specifications. Standard reference temperature for the specification of geometrical and dimensional properties*. ISO catalogue.

[9] International Organization for Standardization. ISO 14253-1:2017, *Geometrical product specifications. Inspection by measurement of workpieces and measuring equipment. Part 1: Decision rules for verifying conformity or nonconformity with specifications*. ISO catalogue.

[10] P. J. Huber. Robust estimation of a location parameter. *The Annals of Mathematical Statistics* 35(1), 73–101, 1964. 10.1214/aoms/1177703732.

[11] A. Savitzky and M. J. E. Golay. Smoothing and differentiation of data by simplified least squares procedures. *Analytical Chemistry* 36(8), 1627–1639, 1964. 10.1021/ac60214a047.

[12] R. J. Hocken and P. H. Pereira, eds. *Coordinate Measuring Machines and Systems*, 2nd ed. CRC Press, 2012. Publisher’s catalogue.

Appendix A. Original figure concordance

The references in this table locate every original technical panel. The manufacturer images are credited at their first appearance. French labels in historical material have been preserved.

Table A.1 – Source [2]. PDF page numbers count the cover.

Source location	Subject	Manuscript
p. 1, Cover	Machine Checking Gauge and probe diagram	Figure 1.1
p. 3, Executive summary	Manufacturer’s product image, as reproduced in the source	Figure 1.3
p. 9, 2.1	Nominal station, measured deviation and probing normal	Figure 1.4
p. 12, 3.1a	MCG installed on the ZEISS machine	Figure 1.2
p. 12, 3.1b	Hand sketch of stylus motion between stations	Figure 1.7
p. 13, 1	Planar positions and normals	Figure 1.5
p. 13, 2	Geometry generation and point validation	Figure 2.3
p. 14, 3	Manufacturer’s operating envelope, as reproduced in the source	Figure 1.6
p. 14, 4a	Nominal spatial stations	Figure 2.1
p. 14, 4b	Nominal probing normals shown in 3D	Figure 2.2
p. 15, 5	Data processing stages	Figure 2.4
p. 18, 4.1a	ZEISS polar trace, 240 points	Figure 3.1
p. 18, 4.1b	ZEISS polar trace, 122 points	Figure 3.2
p. 18, 4.1c	ZEISS polar trace, 120 points, negative direction	Figure 3.3
p. 18, 4.1d	ZEISS polar trace, 120 points, positive direction	Figure 3.4
p. 19, 5.1	Original plan of ordered latitude sweeps	Figure 2.5
p. 20, 5.2	Reference and translated spheres	Figure 4.1
p. 21, 6	Joint estimation workflow proposed in source [2]	Figure 4.2
p. 21, 7	Huber weight law	Figure 4.4
p. 22, 8	Original synthetic recovery error plotted in source [2]	Figure 5.1
p. 24, 6.1	Belt and complementary caps	Figure 6.1
p. 26, 9	Previous simulated filtering example	Figure 6.5

Table A.2 – Additional panels preserved from source [1].

Source location	Subject	Manuscript
I.2	Planar geometry generator and plotting	Figure C.1
I.3	Generator of planar coordinate files	Figure C.2
I.5	Spatial geometry generator and plotting	Figure C.3
I.7	Generator of spherical coordinate files	Figure C.4
Export list	Six text files named by MCG arm length	Figure C.5
Export excerpt	Six-column ZEISS coordinate file example	Figure C.6
Importer	Legacy selection of direction and ring order	Figure C.7
Translation fit	Legacy four-parameter least-squares fit	Figure C.8
Angle fits	Legacy scalar angular fits	Figure C.9
Test generator	Legacy synthetic branches and angle injection	Figure C.10
Filtering listing	MATLAB filtering and subtraction	Figure C.11

Appendix B. Original equations

Facsimiles preserve the mathematical typography of the project records. For use in new analysis, the main text fixes the coordinate convention, temperature interpretation and assumptions of each fit. Source page numbers count the cover.

EN source p. 8 · Measurement function and uncertainty

$$Y = f(X_1, X_2, \dots, X_m),$$

$$\boxed{u_c^2(Y) = \sum_{j=1}^{m} c_j^2 u^2(X_j) + 2 \sum_{j<k} c_j c_k \, u(X_j, X_k)}.$$

$$\boxed{U = k\, u_c},$$

$$\mathbf{p}_i = \begin{bmatrix} x_i & y_i & z_i \end{bmatrix}^{\mathsf{T}}$$

$$\mathbf{n}_i = \begin{bmatrix} n_{x,i} & n_{y,i} & n_{z,i} \end{bmatrix}^{\mathsf{T}}, \qquad \|\mathbf{n}_i\|_2 = 1.$$

EN source p. 9 · Normal projection and parametrisation

$$\boxed{\mathbf{q}_i = \mathbf{p}_i + \varepsilon_i \mathbf{n}_i.}$$

$$\boxed{\mathbf{p}(\theta) = \mathbf{c} + R \begin{bmatrix} \cos\theta \\ \sin\theta \\ 0 \end{bmatrix}, \qquad \mathbf{n}(\theta) = \begin{bmatrix} \cos\theta \\ \sin\theta \\ 0 \end{bmatrix}.}$$

$$\theta_i = \theta_0 + \frac{2\pi i}{N}, \qquad i = 0, \dots, N-1.$$

$$\boxed{\mathbf{p}(\phi, \theta) = \mathbf{c} + R \begin{bmatrix} \cos\phi\cos\theta \\ \cos\phi\sin\theta \\ \sin\phi \end{bmatrix}, \qquad \mathbf{n}(\phi, \theta) = \frac{\mathbf{p}(\phi,\theta) - \mathbf{c}}{R}.}$$

$$-45^\circ \le \phi \le 45^\circ,$$

$$-R\sin 45^\circ \le z - c_z \le R \sin 45^\circ$$

$$\rho(\phi) = R\cos\phi \in [R\cos 45^\circ, R].$$

EN source p. 10 · Associated form and directional statistics

$$(\hat{\mathbf{c}}, \widehat{R}) = \arg\min_{\mathbf{c}, R} \sum_{i=1}^{N} \left(\|\mathbf{q}_i - \mathbf{c}\|_2 - R \right)^2.$$

$$r_i = \|\mathbf{q}_i - \hat{\mathbf{c}}\|_2 - \widehat{R}.$$

$$\boxed{t_{\mathrm{CIR}} = \min_{\mathbf{c}} \left[\max_i \|\mathbf{q}_i - \mathbf{c}\|_2 - \min_i \|\mathbf{q}_i - \mathbf{c}\|_2 \right].}$$

$$\boxed{t_{\mathrm{SPH}} = \min_{\mathbf{c}} \left[\max_i \|\mathbf{q}_i - \mathbf{c}\|_2 - \min_i \|\mathbf{q}_i - \mathbf{c}\|_2 \right],}$$

$$h(\theta_i) = \varepsilon^{+}(\theta_i) - \varepsilon^{-}(\theta_i).$$

$$\boxed{H_{\mathrm{RMS}} = \sqrt{\frac{1}{N} \sum_{i=1}^{N} h^2(\theta_i)}}, \qquad \boxed{H_{\mathrm{pp}} = \max_i h(\theta_i) - \min_i h(\theta_i)},$$

$$\boxed{\overline{h} = \frac{1}{N} \sum_{i=1}^{N} h(\theta_i).}$$

$$\Delta L_T = \alpha_L L \, (T - 20^\circ\mathrm{C}).$$

EN source p. 11 · Additive uncertainty budget

$$\boxed{u_c^2 = u_{\mathrm{CMM}}^2 + u_{\mathrm{probe}}^2 + u_{\mathrm{MCG}}^2 + u_T^2 + u_{\mathrm{repeat}}^2 + u_{\mathrm{fit}}^2 + u_{\mathrm{drift}}^2.}$$

EN source p. 13 · Planar export and discretisation

$$\mathbf{p}_i = \mathbf{c} + R \begin{bmatrix} \cos\theta_i \\ \sin\theta_i \\ 0 \end{bmatrix}, \qquad \theta_i = \theta_0 + \frac{2\pi i}{N},$$
$$\mathbf{n}_i = \frac{\mathbf{p}_i - \mathbf{c}}{\|\mathbf{p}_i - \mathbf{c}\|_2}.$$

$$[\, x_i \; y_i \; z_i \; n_{x,i} \; n_{y,i} \; n_{z,i} \,].$$

$$d_c = 2R \sin\!\left(\frac{\Delta\theta}{2}\right) = 2R \sin\!\left(\frac{\pi}{N}\right).$$

$$N \ge \left\lceil \frac{\pi}{\arcsin(d_{\max}/2R)} \right\rceil.$$

EN source p. 14 · Spatial point generation

$$\mathbf{p}_{i,j} = \mathbf{c} + R \begin{bmatrix} \cos\phi_j \cos\theta_{i,j} \\ \cos\phi_j \sin\theta_{i,j} \\ \sin\phi_j \end{bmatrix}, \qquad \mathbf{n}_{i,j} = \frac{\mathbf{p}_{i,j} - \mathbf{c}}{R}.$$

$$\phi_j = -45^\circ + j \frac{90^\circ}{M-1}, \qquad M = 10,$$

$$\rho_j = R\cos\phi_j, \qquad z_j = R\sin\phi_j.$$

$$N_j = \max\!\left(N_{\min}, \left\lceil \frac{2\pi\rho_j}{d_t} \right\rceil \right).$$

EN source p. 19 · Four-parameter system

$$\boxed{\varepsilon_i = u n_{x,i} + v n_{y,i} + w n_{z,i} + \delta R + \eta_i,}$$

$$\mathbf{x} = \begin{bmatrix} u & v & w & \delta R \end{bmatrix}^{\mathsf{T}}, \qquad A_i = \begin{bmatrix} n_{x,i} & n_{y,i} & n_{z,i} & 1 \end{bmatrix},$$

$$\boldsymbol{\varepsilon} = A\mathbf{x} + \boldsymbol{\eta}.$$

$$\boxed{\hat{\mathbf{x}} = A^{+}\boldsymbol{\varepsilon},}$$

$$\hat{\mathbf{x}} = (A^{\mathsf{T}}A)^{-1}A^{\mathsf{T}}\boldsymbol{\varepsilon}$$

EN source p. 20 · Residual covariance and squareness

$$\hat{\mathbf{r}} = \boldsymbol{\varepsilon} - A\hat{\mathbf{x}}, \qquad \hat{\sigma}^2 = \frac{\|\hat{\mathbf{r}}\|_2^2}{N-p},$$

$$\boxed{\operatorname{Cov}(\hat{\mathbf{x}}) \approx \hat{\sigma}^2 (A^{\mathsf{T}}A)^{-1}.}$$

$$\varepsilon_i \approx u n_{x,i} + v n_{y,i} + w n_{z,i} + \delta R - \alpha z_i n_{y,i} - \beta x_i n_{z,i} - \gamma y_i n_{x,i} + \eta_i.$$

$$\mathbf{q} = \begin{bmatrix} u & v & w & \delta R & \alpha & \beta & \gamma \end{bmatrix}^{\mathsf{T}}$$

$$A_i = \begin{bmatrix} n_{x,i} & n_{y,i} & n_{z,i} & 1 & -z_i n_{y,i} & -x_i n_{z,i} & -y_i n_{x,i} \end{bmatrix}.$$

$$\boxed{\hat{\mathbf{q}} = A^{+}\boldsymbol{\varepsilon}}$$

EN source p. 21 · Scaled fit and robust weights

$$\hat{\mathbf{z}} = \widetilde{A}^{+}\varepsilon, \qquad \hat{\mathbf{q}} = D^{-1}\hat{\mathbf{z}}.$$

$$w_i = \begin{cases} 1, & |u_i| \le c, \\ \dfrac{c}{|u_i|}, & |u_i| > c, \end{cases} \qquad c = 1.345,$$

$$\hat{\mathbf{q}}^{(k+1)} = \arg\min_{\mathbf{q}} \|W_k^{1/2}(A\mathbf{q} - \varepsilon)\|_2^2.$$

$$\operatorname{Cov}(\hat{\mathbf{q}}) \approx \hat{\sigma}^2 (A^T W A)^{-1}.$$

EN source p. 22 · Synthetic validation error

$$\mathbf{e}_{\text{val}} = \mathbf{q}_{\text{estimated}} - \mathbf{q}_{\text{prescribed}}, \qquad E_j = \frac{|e_{\text{val},j}|}{\max(|q_{\text{prescribed},j}|, q_{j,\min})}.$$

EN source p. 24 · Sphere area and original vertical ring spacing

$$A_{\text{zone}} = 2\pi R^2 (\sin\phi_2 - \sin\phi_1).$$

$$A_{\pm 45} = 4\pi R^2 \sin 45^\circ = 2\sqrt{2}\pi R^2.$$

$$\boxed{\frac{A_{\pm 45}}{4\pi R^2} = \sin 45^\circ \approx 70.7\%.}$$

$$z_j = z_{\min} + j\frac{z_{\max} - z_{\min}}{M-1}, \qquad \rho_j = \sqrt{R^2 - z_j^2}.$$

EN source p. 25 · Spacing, direction sequencing and diagnostic filters

$$N_j = \max\left(N_{\min}, \left\lceil \frac{2\pi\rho_j}{d_t} \right\rceil\right).$$

$$A_1 \to B_1 \to B_2 \to A_2,$$

$$m_k = \operatorname{median}_{j \in \mathcal{W}_k}(e_j), \qquad s_k = 1.4826 \operatorname{median}_{j \in \mathcal{W}_k} |e_j - m_k|.$$

$$|e_k - m_k| > 3 s_k.$$

$$\hat{\mathbf{a}}_k = \arg\min_{\mathbf{a}} \sum_{j=-M}^{M} \left[e_{k+j} - \sum_{p=0}^{d} a_p j^p \right]^2, \qquad e_f[k] = \hat{a}_{0,k}.$$

FR source p. 6 · Original coordinate bounds

$$: \ \left[-R.\cos 45\,^\circ ; R.\cos 45\,^\circ \right].$$

$$\text{alle} : \left[R.\sin 45\,^\circ ; R \right].$$

FR source p. 14 · Linearised sphere equation

$$\varepsilon_i = u.x_{\text{ni}} + v.y_{\text{ni}} + w.z_{\text{ni}} + \delta r$$

FR source p. 15 · Least squares and separate angular equations

$$\xi_i = \varepsilon_i - f(u, v, w, \delta r)$$

$$f(u, v, w, \delta r) = u.x_{\text{ni}} + v.y_{\text{ni}} + w.z_{\text{ni}} + \delta r$$

$$\xi_i = 0$$

$$\begin{pmatrix} u \\ v \\ w \\ \delta r \end{pmatrix} = (A^T.A)^{-1}.A^T B$$

$$\xi_i = \varepsilon_i - u.x_{\text{ni}} - v.y_{\text{ni}} - w.z_{\text{ni}} - \delta r - (-\alpha.z.y_{\text{ni}})$$
$$\xi_i = \varepsilon_i - u.x_{\text{ni}} - v.y_{\text{ni}} - w.z_{\text{ni}} - \delta r - (-\beta.x.z_{\text{ni}})$$
$$\xi_i = \varepsilon_i - u.x_{\text{ni}} - v.y_{\text{ni}} - w.z_{\text{ni}} - \delta r - (-\gamma.y.x_{\text{ni}})$$

$$\gamma = (A^T.A)^{-1}.A^T B$$

Appendix C. Original software excerpts

The 2024 French report [1] reproduces the Python listings used to generate and write the coordinates, import the measurements and obtain the stage-by-stage solution. These excerpts are reproduced below, including the progression through the original synthetic generator. The file listing and six-column excerpt are retained as evidence of the export format.

```
"""
IMPORTATIONS DES BIBLIOTHÈQUES NÉCESSAIRES
"""
import numpy as np  # Bibliothèque pour le calcul numérique
import matplotlib.pyplot as plt  # Bibliothèque pour la création de graphiques

"""
DÉCLARATION DES LISTES ET VARIABLES
"""
L_R = [101, 151, 226, 380, 532, 685]  # Liste de toutes les longueurs de bras disponibles en mm
Nb = 60  # nombre de points mesurés sur un cercle
Theta = 2 * np.pi / Nb  # angle entre deux points du cercle
C = [0, 0, 0]  # coordonnées X,Y de la base du cercle
X = []  # Liste pour stocker les coordonnées X des points sur le cercle
Y = []  # Liste pour stocker les coordonnées Y des points sur le cercle
R = L_R[-1]  # Rayon du cercle choisi pour l'affichage

"""
CALCULS DES COORDONNÉES DU CERCLE
"""
# Calcul des coordonnées X et Y des points sur le cercle
X = [R * np.cos(Theta * i) + C[0] for i in range(1, Nb + 1)]
Y = [R * np.sin(Theta * i) + C[1] for i in range(1, Nb + 1)]

# Affichage du cercle
plt.scatter(X, Y, label='Cercle')
plt.axis('equal')  # Ajuster les axes pour qu'ils aient la même échelle
plt.xlabel('X')
plt.ylabel('Y')

"""
CALCULS DES VECTEURS NORMAL DES POINTS DU CERCLE
"""
# Calcul des vecteurs normaux aux points du cercle
normals_x = 5*np.cos(Theta)  # Composante x des vecteurs normaux
normals_y = -5*np.sin(Theta)  # Composante y des vecteurs normaux

# Affichage des vecteurs normaux
plt.quiver(X, Y, normals_x, normals_y, color='r')
plt.legend()
plt.show()
```

Figure C.1 – Planar point and normal generation in the 2024 Python source [1].

```
"""
ÉCRITURE DES COORDONNÉES DANS LES 6 FICHIERS TEXTES POUR LES 6 RAYONS
"""
for R in L_R :

    nom="coordonnees_mesure_bras_"+str(R)+"_plan_normal.txt"

    fichier=open(nom,'w')

    for i in range(1,Nb+1) :
        x=[R * np.sin(Theta * i) + C[1] for i in range(1, Nb + 1)]
        y=-R*np.sin(Theta*i)+C[1]
        z=C[2]
        xn=np.cos(Theta*i)+C[0]
        yn=-np.sin(Theta*i)+C[1]
        zn=C[2]

        fichier.write('{:.7f}'.format(x)+' '+'{:.7f}'.format(y)+' '+'{:.7f}'.format(z)+' '+'{:.7f}'.format(xn)+' '+'{:.7f}'.format(yn)+' '+'{:.7f}'.format(zn)+'\n')


fichier.close() # Fermeture du fichier
```

Figure C.2 – Original loop writing six-column planar sequences for the six arm lengths [1].

```python
" Importation des bibliothèques nécessaires "
import numpy as np                                          # Bibliothèque pour le calcul numérique
import matplotlib.pyplot as plt                             # Bibliothèque pour la création de graphiques
from mpl_toolkits.mplot3d import Axes3D                     # Outils spécifiques pour les graphiques en 3D


" DÉCLARATION DES LISTES ET VARIABLES "
L_R = [101, 151, 226, 380, 532, 685]                        # Liste de toutes les longueurs de bras disponibles en mm
L_H = [31.75, 72, 127, 235]                                 # Liste de toutes les hauteurs de support disponibles en mm
Nb = 60                                                     # nombre de points mesurés sur un cercle du plan horizontal
Theta = 2 * np.pi / Nb                                      # angle entre deux points du cercle
C = [0, 0, 0]                                               # coordonnées X,Y et Z de la base de la sphère
H = 0                                                       # hauteur choisie de support
Nb_Z = 10                                                   # nombre de cercles du plan horizontal différents à mesurer
Phi = np.pi / (2 * Nb_Z)                                    # angle entre deux points dans le plan ZX ou YZ
X = []                                                      # Liste pour stocker les coordonnées X des points sur la sphère
Y = []                                                      # Liste pour stocker les coordonnées Y des points sur la sphère
Z = []                                                      # Liste pour stocker les coordonnées Z des points sur la sphère
R = L_R[-1]                                                 # Rayon de la sphère


" Calcul des coordonnées des points sur la sphère "
for j in range(1, Nb_Z + 1):
    Rphi = R * np.sin(j * Phi + np.pi / 4)                  # Calcul du rayon à une certaine latitude

    X.extend([Rphi * np.cos(Theta * i) + C[0] for i in range(1, Nb + 1)])   # Ajout des coordonnées des points sur le cercle à la liste correspondante
    Y.extend([Rphi * np.sin(Theta * i) + C[1] for i in range(1, Nb + 1)])
    Z.extend([C[2] + H + R * np.cos(j * Phi + np.pi / 4) for i in range(1, Nb + 1)])

fig = plt.figure()                                          # Création d'une nouvelle figure
ax = fig.add_subplot(projection='3d')                       # Ajout de sous-tracés en 3D
ax.scatter(X, Y, Z)                                         #Tracer les points en 3D (Sphère)
normals = np.array([X, Y, Z]) / np.linalg.norm([X, Y, Z], axis=0)   # Calcul des vecteurs normaux à la sphère et normalisation
ax.quiver(X, Y, Z, normals[0]*10, normals[1]*10, normals[2]*10, color='r', length=20) # Tracer les vecteurs normaux avec une longueur multipliée par 10 pour les rendre plus longs
ax.set_xlabel('X')                                          # Étiquette pour l'axe X
ax.set_ylabel('Y')                                          # Étiquette pour l'axe Y
ax.set_zlabel('Z')                                          # Étiquette pour l'axe Z
plt.show()                                                  # Afficher le graphique
```

Figure C.3 – Spherical points and normals generator with plotting and parameters [1].

```python
# Écriture des coordoonnées dans un fichier txt
for R in L_R :  # Pour chaque valeur de rayon R dans la liste L_R

    nom="coordonnees_mesure_bras_"+str(R)+"_sphere.txt"  # Nom du fichier txt basé sur la valeur de R

    fichier=open(nom,'w')  # Ouverture du fichier en mode écriture

    for j in range(1,Nb_Z+1):  # Pour chaque index j de 1 à Nb_Z inclus

        Rphi=R*np.sin(j*Phi+np.pi/4)  # Calcul de Rphi

        for i in range(1,Nb+1) :  # Pour chaque index i de 1 à Nb inclus
            x=-Rphi*np.cos(Theta*i)+C[0]  # Calcul de la coordonnée x
            y=Rphi*np.sin(Theta*i)+C[1]   # Calcul de la coordonnée y
            z=C[2]+H+R*np.cos(j*Phi+np.pi/4)  # Calcul de la coordonnée z
            xn=np.sin(j*Phi+np.pi/4)*np.cos(Theta*i)+C[0]  # Calcul de la coordonnée x de la normale
            yn=np.sin(j*Phi+np.pi/4)*np.sin(Theta*i)+C[1]  # Calcul de la coordonnée y de la normale
            zn=np.cos(j*Phi+np.pi/4)+C[2]  # Calcul de la coordonnée z de la normale
            # Écriture des coordonnées et des coordonnées normales dans le fichier
            fichier.write('{:.7f}'.format(x)+' '+'{:.7f}'.format(y)+' '+'{:.7f}'.format(z)+' '+'{:.7f}'.format(xn)+' '+'{:.7f}'.format(yn)+' '+'{:.7f}'.format(zn)+'\n')

# Fermeture du fichier
fichier.close()
```

Figure C.4 – Original loop writing six-column spatial sequences [1].

coordonnees_mesure_bras_101_sphere.txt	aujourd'hui à 22:28	39 ko	Format texte
coordonnees_mesure_bras_151_sphere.txt	aujourd'hui à 22:28	40 ko	Format texte
coordonnees_mesure_bras_226_sphere.txt	aujourd'hui à 22:28	41 ko	Format texte
coordonnees_mesure_bras_380_sphere.txt	aujourd'hui à 22:28	41 ko	Format texte
coordonnees_mesure_bras_532_sphere.txt	aujourd'hui à 22:28	41 ko	Format texte
coordonnees_mesure_bras_685_sphere.txt	aujourd'hui à 22:28	41 ko	Format texte

Figure C.5 – Files generated for the six nominal arm lengths as shown in the 2024 report [1].

coordonnees_mesure_bras_151_sphere.txt

```
-121.4923523 12.7693608 88.7555731 0.8045851 0.0845653 0.5877853
-119.4920428 25.3988178 88.7555731 0.7913380 0.1682041 0.5877853
-116.1825535 37.7500000 88.7555731 0.7694209 0.2500000 0.5877853
-111.6001439 49.6875853 88.7555731 0.7390738 0.3290569 0.5877853
-105.7950197 61.0807831 88.7555731 0.7006293 0.4045085 0.5877853
-98.8307831 71.8047670 88.7555731 0.6545085 0.4755283 0.5877853
-90.7837358 81.7420428 88.7555731 0.6012168 0.5413380 0.5877853
-81.7420428 90.7837358 88.7555731 0.5413380 0.6012168 0.5877853
-71.8047670 98.8307831 88.7555731 0.4755283 0.6545085 0.5877853
-61.0807831 105.7950197 88.7555731 0.4045085 0.7006293 0.5877853
-49.6875853 111.6001439 88.7555731 0.3290569 0.7390738 0.5877853
-37.7500000 116.1825535 88.7555731 0.2500000 0.7694209 0.5877853
-25.3988178 119.4920428 88.7555731 0.1682041 0.7913380 0.5877853
-12.7693608 121.4923523 88.7555731 0.0845653 0.8045851 0.5877853
-0.0000000 122.1615662 88.7555731 0.0000000 0.8090170 0.5877853
12.7693608 121.4923523 88.7555731 -0.0845653 0.8045851 0.5877853
25.3988178 119.4920428 88.7555731 -0.1682041 0.7913380 0.5877853
37.7500000 116.1825535 88.7555731 -0.2500000 0.7694209 0.5877853
49.6875853 111.6001439 88.7555731 -0.3290569 0.7390738 0.5877853
61.0807831 105.7950197 88.7555731 -0.4045085 0.7006293 0.5877853
71.8047670 98.8307831 88.7555731 -0.4755283 0.6545085 0.5877853
81.7420428 90.7837358 88.7555731 -0.5413380 0.6012168 0.5877853
90.7837358 81.7420428 88.7555731 -0.6012168 0.5413380 0.5877853
98.8307831 71.8047670 88.7555731 -0.6545085 0.4755283 0.5877853
105.7950197 61.0807831 88.7555731 -0.7006293 0.4045085 0.5877853
111.6001439 49.6875853 88.7555731 -0.7390738 0.3290569 0.5877853
116.1825535 37.7500000 88.7555731 -0.7694209 0.2500000 0.5877853
119.4920428 25.3988178 88.7555731 -0.7913380 0.1682041 0.5877853
121.4923523 12.7693608 88.7555731 -0.8045851 0.0845653 0.5877853
```

Figure C.6 – Excerpt of the 151 mm nominal coordinate file, with three spatial coordinates and three components of the normal [1].

```
def importer_donnees(nom_fichier): #importe les donnees du fichier dans le même dossier que le fichier .py
    file=open(nom_fichier,'r')
    L_lignes=file.readlines()
    Nx,Ny,Nz,E=[],[],[],[]
    MA,MB=[],[]
    Y,X,Z=[],[],[]
    imax=len(L_lignes)/2
    # print(imax)
    i=0
    for L in L_lignes :

        q=i//60        #sert à choisir quels cercles de mesure on étudie parmi tous les allers retours faits
        if q%2==0 : # == -> cercles impairs (sens horaire), != -> cercles pairs (sens anti-horaire)
            i+=1
            continue
        if i > imax :  # <= -> retour, > -> aller
            i+=1
            continue
        i+=1
        L=L.strip()
        L=L.split(" ")
        nx=float(L[3])
        ny=float(L[4])
        nz=float(L[5])
        e=float(L[6])
        y=float(L[1])
        x=float(L[0])
        z=float(L[2])
        Nx.append(nx)
        Ny.append(ny)
        Nz.append(nz)
        X.append(x)
        Y.append(y)
        Z.append(z)
        E.append(e)
        MA.append([nx,ny,nz,1])
        MB.append([e])
    file.close()
    return Nx,Ny,Nz,E,MA,MB,X,Y,Z
```

Figure C.7 – Original importer with 60-row ring indexing, parity selection, half-file split and positional parsing [1].

```
def systeme(nom): #renvoie la liste des u,v,w et dr
    XN,YN,ZN,E,MA,MB,X,Y,Z=importer_donnees(nom)
    Msol=np.linalg.lstsq(MA,MB)
    # print(Msol)
    u,v,w,dr=float(Msol[0][0]),float(Msol[0][1]),float(Msol[0][2]),float(Msol[0][3])
    return u,v,w,dr
```

Figure C.8 – Original four-parameter least-squares routine [1].

The importer’s index assumes that each source block is already correctly oriented and has exactly 60 rows. When an endpoint is repeated or a row omitted, an explicit ring and traversal ID is more reliable. The stored loops below show which conventions would need to be reconstructed for a comparison with the original fit.

```
def systeme_gamma(nom): #renvoie l'angle de décalage entre deux axes Gamma
    XN,YN,ZN,E,MA,MB,X,Y,Z=importer_donnees(nom)
    u,v,w,dr=systeme(nom)
    MS=[[-E[i]+u*XN[i]+v*YN[i]+w*ZN[i]+dr] for i in range(len(E))]
    LY=[[Y[i]*XN[i]] for i in range(len(Y))]
    LYinv=[[Y[i]*XN[i] for i in range(len(Y))]]
    a=np.dot(LYinv,LY)
    b=np.dot(LYinv,MS)
    gamma=b/a
    return "gamma = "+str(float(gamma))

def systeme_alpha(nom): #renvoie l'angle de décalage entre deux axes Gamma
    XN,YN,ZN,E,MA,MB,X,Y,Z=importer_donnees(nom)
    u,v,w,dr=systeme(nom)
    MS=[[-E[i]+u*XN[i]+v*YN[i]+w*ZN[i]+dr] for i in range(len(E))]
    LZ=[[Z[i]*YN[i]] for i in range(len(Y))]
    LZinv=[[Z[i]*YN[i] for i in range(len(Y))]]
    a=np.dot(LZinv,LZ)
    b=np.dot(LZinv,MS)
    alpha=b/a
    return "alpha = "+str(float(alpha))

def systeme_beta(nom): #renvoie l'angle de décalage entre deux axes Gamma
    XN,YN,ZN,E,MA,MB,X,Y,Z=importer_donnees(nom)
    u,v,w,dr=systeme(nom)
    MS=[[-E[i]+u*XN[i]+v*YN[i]+w*ZN[i]+dr] for i in range(len(E))]
    LX=[[X[i]*ZN[i]] for i in range(len(Y))]
    LXinv=[[X[i]*ZN[i] for i in range(len(Y))]]
    a=np.dot(LXinv,LX)
    b=np.dot(LXinv,MS)
    beta=b/a
    return "beta = "+str(float(beta))
```

Figure C.9 – Original three independent angular fits. The three dot products use Y times n_x, Z times n_y and X times n_z [1].

```
def cootest(dr,u,v,w,gamma,alpha,beta):
    nom="coordonnees_test.txt"
    fichier=open(nom,'w')
    R=Rt+dr
    C=[0,0,0]
    for j in range(0,Nb_Z):

        Rphi=R*np.sin(j*Phi+np.pi/4)

        for i in range(1,Nb+1) :
            x=Rphi*np.cos(Theta*i)+C[0]
            y=Rphi*np.sin(Theta*i)+C[1]
            z=C[2]+H+R*np.cos(j*Phi+np.pi/4)
            xn=np.sin(j*Phi+np.pi/4)*np.cos(Theta*i)+C[0]*0 #coordonnees xn et yn du Vecteur normal
            yn=np.sin(j*Phi+np.pi/4)*np.sin(Theta*i)+C[1]*0 #a la sphere au point XYZ
            zn=np.cos(j*Phi+np.pi/4)+C[2]*0
            e=xn*u+yn*v+zn*w+dr
            fichier.write('{:.7f}'.format(x)+' '+'{:.7f}'.format(y)+' '+'{:.7f}'.format(z)+' '+'{:.7

        for i in reversed(range(1,Nb+1)) :
            x=Rphi*np.cos(Theta*i)+C[0]
            y=Rphi*np.sin(Theta*i)+C[1]
            z=C[2]+H+R*np.cos(j*Phi+np.pi/4)
            xn=np.sin(j*Phi+np.pi/4)*np.cos(Theta*i)+C[0]*0
            yn=np.sin(j*Phi+np.pi/4)*np.sin(Theta*i)+C[1]*0
            zn=np.cos(j*Phi+np.pi/4)+C[2]*0
            e=xn*u+yn*v+zn*w+dr-y*xn*gamma-z*yn*alpha-x*zn*beta

            fichier.write('{:.7f}'.format(x)+' '+'{:.7f}'.format(y)+' '+'{:.7f}'.format(z)+' '+'{:.7

    for j in reversed(range(0,Nb_Z)):

        Rphi=R*np.sin(j*Phi+np.pi/4)

        for i in range(1,Nb+1) :
            x=Rphi*np.cos(Theta*i)+C[0]
            y=Rphi*np.sin(Theta*i)+C[1]
            z=C[2]+H+R*np.cos(j*Phi+np.pi/4)
            xn=np.sin(j*Phi+np.pi/4)*np.cos(Theta*i)+C[0]*0 #coordonnees xn et yn du Vecteur normal
            yn=np.sin(j*Phi+np.pi/4)*np.sin(Theta*i)+C[1]*0 #a la sphere au point XYZ
            zn=np.cos(j*Phi+np.pi/4)+C[2]*0
            e=xn*u+yn*v+zn*w+dr-y*xn*gamma-z*yn*alpha-x*zn*beta
            fichier.write('{:.7f}'.format(x)+' '+'{:.7f}'.format(y)+' '+'{:.7f}'.format(z)+' '+'{:.7

        for i in reversed(range(1,Nb+1)) :
            x=Rphi*np.cos(Theta*i)+C[0]
            y=Rphi*np.sin(Theta*i)+C[1]
            z=C[2]+H+R*np.cos(j*Phi+np.pi/4)
            xn=np.sin(j*Phi+np.pi/4)*np.cos(Theta*i)+C[0]*0
            yn=np.sin(j*Phi+np.pi/4)*np.sin(Theta*i)+C[1]*0
            zn=np.cos(j*Phi+np.pi/4)+C[2]*0
            e=xn*u+yn*v+zn*w+dr-y*xn*gamma-z*yn*alpha-x*zn*beta
            fichier.write('{:.7f}'.format(x)+' '+'{:.7f}'.format(y)+' '+'{:.7f}'.format(z)+' '+'{:.7

    fichier.close()
```

Figure C.10 – Original `cootest` listing. In the first loop, the scalar residual ends after the radius term. The next three loops include the shear terms [1].

The three original angular routines form one signed residual from the estimated translation and radius before each scalar fit. Equation (4.6) gives the corresponding joint elimination with projected

angular columns. The MATLAB listing implements a different stage, acting on the stored coordinate and normal fields.

Editor - D:\OPM\lissage.m

lissage.m

```
% Lire les données théoriques
data_theorique = load('theorique.txt');
x = data_theorique(:, 1);
y = data_theorique(:, 2);
z = data_theorique(:, 3);
xn = data_theorique(:, 4);
yn = data_theorique(:, 5);
zn = data_theorique(:, 6);
% Lire les données expérimentales
data_experimentale = load('experimentale.txt');
x2 = data_experimentale(:, 1);
y2 = data_experimentale(:, 2);
z2 = data_experimentale(:, 3);
xn2 = data_experimentale(:, 4);
yn2 = data_experimentale(:, 5);
zn2 = data_experimentale(:, 6);
% Calcul des écarts
dx = x2 - x;
dy = y2 - y;
dz = z2 - z;
dxn = xn2 - xn;
dyn = yn2 - yn;
dzn = zn2 - zn;
% Appliquer un filtre de moyenne mobile sur les écarts
window_size = 5; % Taille de la fenêtre de moyenne mobile
dx_smooth = movmean(dx, window_size);
dy_smooth = movmean(dy, window_size);
dz_smooth = movmean(dz, window_size);
dxn_smooth = movmean(dxn, window_size);
dyn_smooth = movmean(dyn, window_size);
dzn_smooth = movmean(dzn, window_size);
% Correction des coordonnées expérimentales
x2_corrected = x2 - dx_smooth;
y2_corrected = y2 - dy_smooth;
z2_corrected = z2 - dz_smooth;
xn2_corrected = xn2 - dxn_smooth;
yn2_corrected = yn2 - dyn_smooth;
zn2_corrected = zn2 - dzn_smooth;
% Enregistrer les données corrigées
corrected_data = [x2_corrected, y2_corrected, z2_corrected, xn2_corrected, yn2_corrected, zn2_corrected];
save('experimentale_corrigee.txt', 'corrected_data', '-ascii');
```

Figure C.11 – Original five-sample moving-average subtraction of coordinate and normal-component errors [1].

Appendix D. Reproducibility and data fields

The embedded file `cmm_verification_study.py` was run with Python 3.12.14, NumPy 2.3.5, SciPy 1.17.0 and Matplotlib 3.10.8. It recreates the nine new vector figures, the calculation results in `cmm_results.json` and the reference-only geometry example `nominal_belt_example.csv`. In a standalone PDF reader use the attachment panel, or run the command shown below after extracting the Python file. The master seed is 240410. Independent substreams control the robust, sample-count, timing and filtering experiments. No raw measurement records are required to rerun these comparisons.

```
python cmm_verification_study.py --out results
```

The project references `generation_points_theorique.py`, `resolution_numerique.py` and `coordonnees_theorique.py`, with a spherical variant named in [1]. It records `coordonnees_theorique.txt`, `coordonnees_test.txt` and `SphereAllerRetour_10042024.txt`. Those complete Python listings and measurement files were unavailable. The surviving screenshot excerpts appear in Appendix C. The preserved `Lissage.m` copy performs the same operations shown in Figure C.11. The embedded source PDFs contain the complete reports [1, 2], including page-level context for the original values and equations.

The nominal geometry example uses local coordinates in millimetres and 600 samples for one pass on the archived grid. It lacks timestamps, trigger behaviour, clearance validation and registration to any real CMM. It serves as the input to the identification model. For an actual campaign, record the following fields at an appropriate analysis level.

Table D.1 – Data record recommended for repeatable MCG campaigns.

Level	Fields
Campaign	CMM and controller identifiers, software version, artefact and calibration IDs, probe and stylus configuration.
Run	Run start and end, time zone, pivot and local frame, arm and temperature records, qualification ID, speed and acceleration, procedure version.
Station	Visit and nominal IDs, timestamp, azimuth, elevation, direction, vertical order, nominal position and normal, measured normal deviation, unit and validity flag.
Result	Reconstructed point, common association and filter settings, residual statistics, scaled rank and condition, uncertainty components and decision rule.